

## DEUTERIUM BURNING IN MASSIVE GIANT PLANETS AND LOW-MASS BROWN DWARFS FORMED BY CORE-NUCLEATED ACCRETION

PETER BODENHEIMER<sup>1</sup>, GENNARO D'ANGELO<sup>2,4,5</sup>, JACK J. LISSAUER<sup>2</sup>, JONATHAN J. FORTNEY<sup>1</sup>, AND DIDIER SAUMON<sup>3</sup>

*Accepted for publication in The Astrophysical Journal*

### ABSTRACT

Formation of bodies near the deuterium-burning limit is considered by detailed numerical simulations according to the core-nucleated giant planet accretion scenario. The objects, with heavy-element cores in the range 5–30  $M_{\oplus}$ , are assumed to accrete gas up to final masses of 10–15 Jupiter masses ( $M_{\text{Jup}}$ ). After the formation process, which lasts 1–5 Myr and which ends with a ‘cold-start’, low-entropy configuration, the bodies evolve at constant mass up to an age of several Gyr. Deuterium burning via proton capture is included in the calculation, and we determined the mass,  $M_{50}$ , above which more than 50% of the initial deuterium is burned. This often-quoted borderline between giant planets and brown dwarfs is found to depend only slightly on parameters, such as core mass, stellar mass, formation location, solid surface density in the protoplanetary disk, disk viscosity, and dust opacity. The values for  $M_{50}$  fall in the range 11.6–13.6  $M_{\text{Jup}}$ , in agreement with previous determinations that do not take the formation process into account. For a given opacity law during the formation process, objects with higher core masses form more quickly. The result is higher entropy in the envelope at the completion of accretion, yielding lower values of  $M_{50}$ . For masses above  $M_{50}$ , during the deuterium-burning phase, objects expand and increase in luminosity by 1 to 3 orders of magnitude. Evolutionary tracks in the luminosity–versus–time diagram are compared with the observed position of the companion to Beta Pictoris.

*Keywords:* planet formation; giant planets; brown dwarfs; extrasolar planets

### 1. INTRODUCTION

There is considerable debate over the question of defining a precise boundary between the class of objects known as ‘planets’ and those known as ‘brown dwarfs’. It has been suggested that the two types of objects could be distinguished by their formation mechanism; however, it is generally difficult to deduce this property from observations of specific objects. Nevertheless, there is a well-defined minimum in the mass distribution (actually  $M \sin i$ ), for substellar companions to G and K main-sequence stars, in the range 20–30  $M_{\text{Jup}}$  (Lovis et al. 2006; Sahlmann et al. 2011; Schneider et al. 2011), suggesting that objects near the deuterium-burning limit can ‘form like planets’. These authors suggest that this minimum does correspond to a (somewhat imprecise) dividing line between formation mechanisms and that the upper limit to planet masses should be set at about  $M \sin i \approx 25 M_{\text{Jup}}$ . However, no break is seen near this mass in the distribution of free-floating objects observed in the Sigma Orionis young cluster (Peña Ramírez et al. 2012) down to 4  $M_{\text{Jup}}$ . Together, the observations imply that formation mechanisms do not define a unique mass boundary between planets and brown dwarfs.

Another commonly used criterion to classify planets, brown dwarfs and stars is based on nuclear fusion that does or does not occur within the object. Brown dwarfs are defined to be those objects that at some point in their evolution become hot enough in their interiors to burn a majority of the deuterium that was initially present in the object; however, they never become hot enough to burn  $^1\text{H}$  by the proton-plus-proton reaction in a self-sustaining manner as true stars do. On the other hand, the term planet is applied only to objects that will not burn much deuterium. This criterion was used by Burrows et al. (1997) to separate the two types of objects, and the dividing line was stated to be  $\sim 13 M_{\text{Jup}}$ , where  $M_{\text{Jup}} = 1.898 \times 10^{30}$  g. This dividing line depends on the helium mass fraction, the deuterium abundance, and the metallicity, and Spiegel et al. (2011) found that for a reasonable range of parameters, 50% of the initial D is burned in the mass range 12–14  $M_{\text{Jup}}$ . The evolutionary models used to establish the criterion have a uniform chemical composition, a defined total mass in the vicinity of the 13  $M_{\text{Jup}}$  limit, constant in time, an initial radius of about 2–3  $R_{\text{Jup}}$  where  $R_{\text{Jup}} = 7.15 \times 10^9$  cm, and an initial photospheric temperature ( $T_{\text{eff}}$ ) of about 2500 K. The corresponding initial luminosities are  $2\text{--}3 \times 10^{-3} L_{\odot}$ . A starting model of this type has become known as a ‘hot-start’ model, characterized by a relatively high initial entropy (Marley et al. 2007).

The question of whether, either for brown dwarfs or planets, the formation mechanism actually leads to such hot-start initial conditions is still under investigation. For objects formed either by collapse of interstellar clouds or by fragmentation in a protostellar disk by gravitational instability, it is plausible that the hot-start initial condition could be reached (Baraffe et al. 2002). In

<sup>1</sup>UCO/Lick Observatory, Department of Astronomy and Astrophysics, University of California, Santa Cruz, CA 95064 (E-mail: [peter@ucolick.org](mailto:peter@ucolick.org), [jfortney@ucolick.org](mailto:jfortney@ucolick.org))

<sup>2</sup>Space Science and Astrobiology Division, NASA Ames Research Center, Moffett Field, CA 94035 (E-mail: [gennaro.dangelo@nasa.gov](mailto:gennaro.dangelo@nasa.gov), [Jack.J.Lissauer@nasa.gov](mailto:Jack.J.Lissauer@nasa.gov))

<sup>3</sup>Los Alamos National Laboratory, P. O. Box 1663, Los Alamos, NM 87545 (E-mail: [dsaumon@lanl.gov](mailto:dsaumon@lanl.gov))

<sup>4</sup>SETI Institute, 189 Bernardo Avenue, Mountain View, CA 94043

<sup>5</sup>Visiting Research Scientist, Los Alamos National Laboratory, Los Alamos, NM 87545

the case of gravitational instability, [Galvagni et al. \(2012\)](#) have found, from three-dimensional numerical simulations, that the entropy of newly-formed clumps, near the point where molecular dissociation sets in at the center, is high, possibly consistent with a hot start. However the dominant process for giant planet formation is most likely the core-nucleated accretion mechanism, in which solid particles first accumulate to form a heavy-element core, then later when the core has attained roughly 5–10  $M_{\oplus}$ , gas is captured from the disk. A particular set of evolutionary calculations based on this theory ([Marley et al. 2007](#)) shows that once the planet has become fully formed, its entropy is relatively low, with luminosities on the order of  $10^{-5} - 10^{-6} L_{\odot}$ . The low entropy is a direct consequence of the assumption made in these calculations that, during the phase of rapid gas accretion, all of the accretion energy is radiated away at the accretion shock at the planet's surface. Thus, the core accretion process can lead to a 'cold start'. However the shock treatment is approximate, and the accretion flow cannot actually be modelled correctly with 1-D spherically symmetric calculations. Thus other possibilities can arise. [Mordasini et al. \(2012\)](#) show that core accretion formation calculations in which none of the energy is radiated at the shock lead to hot-start conditions very similar to those assumed by [Baraffe et al. \(2003\)](#) and [Burrows et al. \(1997\)](#). Furthermore, intermediate 'warm' states are also possible outcomes ([Spiegel & Burrows 2012](#)). In the core-accretion picture, also, the chemical composition is not uniform because of the presence of the core, which turns out for the case of a Jupiter mass planet to fall in the range 4–20  $M_{\oplus}$  ([Movshovitz et al. 2010](#)).

A massive object of 25  $M_{\text{Jup}}$  formed by core accretion ([Baraffe et al. 2008](#)) has been shown to burn all of its initial deuterium despite the presence of a heavy-element core of 100 or a few hundred  $M_{\oplus}$ . Cold-start models, including the core and calculations of the formation phase, have been investigated to determine the D-burning mass limit ([Mollière & Mordasini 2012](#)). The results show that the limit still falls within the range 12–14  $M_{\text{Jup}}$ . The purpose of the present paper is to present further formation calculations for bodies formed by core-nucleated accretion that end up with a total mass in the 10–15  $M_{\text{Jup}}$  range in the low-entropy state, and to investigate the effect of various possible initial conditions, as well as physical parameters during the formation stage, on the corresponding deuterium-burning limit.

## 2. COMPUTATIONAL METHOD

The evolutionary calculations for giant planets are started at the point where the heavy-element core has a mass of about 1  $M_{\oplus}$ , and are carried through the entire formation process as well as the subsequent contraction/cooling phase at constant mass, up to a final age of several Gyr. The assumptions and computational procedures were described in detail in previous publications ([Pollack et al. 1996](#); [Bodenheimer et al. 2000](#); [Hubickyj et al. 2005](#); [Lissauer et al. 2009](#); [Movshovitz et al. 2010](#)). The early phase of the formation process is dominated by the accretion of planetesimals onto the core; during this phase the gaseous envelope has low mass,  $\ll 1 M_{\oplus}$ , and a low accretion rate compared to that of the core.

The latter is given by

$$\frac{dM_{\text{core}}}{dt} = \pi R_{\text{capt}}^2 \sigma \Omega_p F_g \quad (1)$$

where  $\pi R_{\text{capt}}^2$  is the effective geometrical capture cross section,  $\sigma$  is the surface density of solid particles (planetesimals) in the protoplanetary disk,  $\Omega_p$  is the planet's orbital frequency, and  $F_g$  is the gravitational enhancement factor, which is obtained from the calculations of [Greenzweig & Lissauer \(1992\)](#). The planetesimal radius is taken to be 50 km for the cases with a central star of 2  $M_{\odot}$  and 100 km for the cases with a star of 1  $M_{\odot}$  (see [Table 1](#)). The smaller size, or a reasonable distribution of planetesimal sizes, tends to reduce the formation time but has little effect on the basic results of this paper.

If no gaseous envelope is present, then  $R_{\text{capt}} = R_{\text{core}}$ , the radius of the heavy-element core. However, even if the envelope mass is relatively small compared with the core mass, the planetesimals interact with the envelope gas, are slowed down by gas drag, and are subject to ablation and fragmentation. The trajectories of planetesimals through the envelope are calculated ([Podolak et al. 1988](#)), and the effective  $R_{\text{capt}}$  is determined. The material that is deposited in the envelope is then allowed to sink to the core, as discussed by [Pollack et al. \(1996\)](#). Calculations by [Iaroslavitz & Podolak \(2007\)](#) show that this assumption is valid at least for the organic and rock components of the planetesimals. The ices, however, can dissolve in the envelope, so that our 'core mass' is somewhat overestimated; the quoted value actually refers to the total excess of heavy-element material, above the solar abundance, in the entire planet. Erosion of the core and possible mixing of some core material into the envelope is not considered. This process has been shown to be unlikely for the case of Jupiter ([Lissauer & Stevenson 2007](#)), but such estimates have not been extended to the case of planets in the 10  $M_{\text{Jup}}$  range.

The structure of the hydrogen-helium envelope is calculated according to the differential equations of stellar structure ([Kippenhahn & Weigert 1990](#)), which assume hydrostatic equilibrium, a spherically symmetric mass distribution, radiative or convective energy transport, and energy conservation. The energy sources are provided by planetesimal accretion, contraction of the gaseous envelope, and cooling. The additional energy source provided by deuterium burning is included in the later phases of accretion and during the constant-mass final cooling phase, once the mass has exceeded 10  $M_{\text{Jup}}$  and internal temperatures exceed  $\approx 10^5$  K. The full set of equations, supplemented by calculation of the mass accretion rates onto the core and the envelope, and of the planetesimal trajectories, is solved by the Henyey method ([Henyey et al. 1964](#)).

At the inner boundary of the envelope the radius is set to  $R_{\text{core}}$ , which is determined from its mean density. During the earlier phases of the evolution, when the envelope mass is less than about 0.1  $M_{\text{Jup}}$ , the core is assumed to be a mixture of rock and ice with a mean density of  $3.0 \text{ g cm}^{-3}$ . During the later phases, when the pressure at the base of the envelope increases to values above  $\sim 10^{11} \text{ dynes cm}^{-2}$ , an ANEOS equation of state with 50% rock and 50% ice ([Thompson 1990](#)) for the core is used to determine its mean density, which can

increase to  $60 \text{ g cm}^{-3}$  or higher. In the hydrogen-helium envelope, the equation of state is taken to be given by the tables of [Saumon, Chabrier, & van Horn \(1995\)](#), which take into account the partial degeneracy of the electrons as well as non-ideal effects. The chemical composition is taken to be near-solar, with  $X = 0.70$ ,  $Y = 0.283$ , and  $Z = 0.017$ , where  $X$ ,  $Y$ ,  $Z$  are, respectively, the mass fractions of hydrogen, helium, and heavy elements. The tables of course do not include a  $Z$  component, so the  $Y$  component was adjusted upwards to partially compensate.

The Rosseland mean opacity during the formation phase combines the low-temperature atomic/molecular calculation of [Alexander & Ferguson \(1994\)](#) with the interstellar grain opacities of [Pollack et al. \(1985\)](#). The opacity values of the grain component are reduced by a factor 50 to approximately represent the reduction caused by grain growth and settling in the protoplanet ([Podolak 2003](#); [Movshovitz & Podolak 2008](#)). However, in two of the runs the grain growth and settling are calculated in detail in the temperature range 100–1800 K as described in [Movshovitz et al. \(2010\)](#). The grain size distributions and the opacities are recalculated in every layer at every time step in that temperature range. These opacities are important in regulating the rate at which the envelope can contract, and therefore the rate at which it accretes gas. However, once the envelope is well into the rapid gas accretion phase, at about  $0.25 M_{\text{Jup}}$ , the gas accretion rate is limited by the physical properties of the protoplanetary disk near the planet, and the precise values of envelope opacity assume a less-important role. Once the planet reaches its final mass, say  $12 M_{\text{Jup}}$ , the grains are assumed to settle rapidly and to evaporate in the interior. For the final contraction/cooling phase at constant mass, the molecular opacities of [Freedman et al. \(2008\)](#) are used, with solar composition, up to a temperature of 3500 K. At and above that temperature, with any reasonable opacity, the interior is convective.

At the outer surface of the envelope, the mass addition rate of gas, during the earlier phases of accretion, is determined by the requirement that the planet radius  $R_p$  match the effective accretion radius, which is given by ([Lissauer et al. 2009](#))

$$R_{\text{eff}} = \frac{GM_p}{c_s^2 + \frac{GM_p}{KR_H}}, \quad (2)$$

where  $c_s$  is the sound speed in the disk,  $R_H$  is the Hill sphere radius, and  $M_p$  is the total mass of the planet. The constant  $K \approx 0.25$  is determined by three-dimensional numerical simulations which calculate the accretion rate of gas from the protoplanetary disk onto the planet ([Lissauer et al. 2009](#)). As a result, in the limit where  $R_H$  is small compared with the Bondi accretion radius  $GM_p/c_s^2$ ,  $R_{\text{eff}} = 0.25R_H$ .

Additional boundary conditions at the surface depend on the evolutionary phase. During the early phases when  $M_p < 0.25 M_{\text{Jup}}$ , the density and temperature are set to constant values appropriate for the protoplanetary disk,  $\rho_{\text{neb}}$  and  $T_{\text{neb}}$ , respectively. The density  $\rho_{\text{neb}}$  is determined from the assumed value of  $\sigma$  using a standard gas-to-solid ratio of 70 and  $H_p/a_p = 0.05$ , where  $H_p$  is the (gaussian) disk scale height and  $a_p$  is the distance of the planet from the star. However at some point

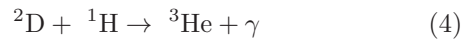
during the rapid gas accretion phase, the mass addition rate required by condition (2) exceeds the rate at which matter can be supplied by the disk. The disk-limited rates, based on three-dimensional hydrodynamic simulations, are described in the next section. During that phase, the boundary conditions at the actual surface of the planet, whose radius falls well below  $R_{\text{eff}}$ , are determined through the properties of the accretion shock at this surface, as described in detail by [Bodenheimer et al. \(2000\)](#). The basic assumption is that practically all of the gravitational energy released by the infalling gas is radiated away at the shock; this energy escapes through the infalling envelope ahead of the shock. This assumption defines the ‘cold start’ for planetary evolution.

During the final phase of cooling at constant mass, the planet becomes isolated from the disk and the surface boundary conditions change again, to those of a blackbody in hydrostatic equilibrium

$$L = 4\pi R_p^2 \sigma_B T_{\text{eff}}^4 \quad \text{and} \quad \kappa P = \frac{2}{3} g, \quad (3)$$

where  $\sigma_B$  is the Stefan-Boltzmann constant,  $T_{\text{eff}}$  is the surface temperature,  $L$  is the total luminosity, and  $\kappa$ ,  $P$ , and  $g$  are, respectively, the photospheric values of Rosseland mean opacity, pressure, and acceleration of gravity. Insolation from the star is not included.

Significant deuterium burning in the mass range considered begins near the end of the phase of rapid gas accretion. The burning occurs via the reaction



with an energy release  $Q_{\text{dp}} = 5.494$  MeV per reaction. The initial deuterium abundance by mass fraction is set to  $4 \times 10^{-5}$ , consistent with the value derived from the local interstellar medium ([Prodanović et al. 2010](#)). The reaction rate (reactions per second per gram) is taken from the Nuclear Astrophysics Compilation of Reaction Rates ([Angulo et al. 1999](#)):

$$R_{\text{dp}}(\rho, T_6) = \frac{5.365 \times 10^{28} \rho X_{1\text{H}} X_{2\text{H}}}{T_6^{2/3}} \exp(-37.21/T_6^{1/3}) \\ \{1 + T_6[0.0143 + T_6(3.95 \times 10^{-7} T_6 - 9.05 \times 10^{-5})]\}, \quad (5)$$

where  $T_6$  is the temperature in  $10^6$  K,  $\rho$  is the density in cgs,  $X_{1\text{H}}$  is the mass fraction of  ${}^1\text{H}$ , and  $X_{2\text{H}}$  is the mass fraction of  ${}^2\text{H}$  (deuterium). This rate is then multiplied by the screening factor, which takes into account ion-ion and ion-electron screening in partially degenerate dense plasmas ([Potekhin & Chabrier 2012](#)). The energy generation  $\epsilon$ , per gram per second, is then obtained, zone by zone, from the rate multiplied by  $Q_{\text{dp}}$  in the appropriate units. To get the change in the deuterium abundance during one time step, it is assumed that the planet interior is fully convective and therefore fully mixed. This assumption is valid for the planets considered during the phase of contraction and cooling, even if no deuterium is burned. The convective velocities of order  $10\text{--}100 \text{ cm s}^{-1}$ , calculated according to the mixing-length approximation, give a mixing time scale far shorter than the D-burning time scale. The reaction rate multiplied by zone mass is integrated over the entire envelope and used to calculate the abundance change.

Given the central stellar mass  $M_*$ , the solid surface density  $\sigma$ , and the distance of the planet from the star  $a_p$ , the isolation mass for the solid material is

$$M_{\text{iso}} = \frac{8}{\sqrt{3}}(\pi C)^{3/2} M_*^{-1/2} \sigma^{3/2} a_p^3 \quad (6)$$

where  $C$  is the number of Hill-sphere radii on each side of the planetary core from which it is able to capture planetesimals;  $C = 4$  in our simulations. Once the core mass approaches  $M_{\text{iso}}$ , the  $dM_{\text{core}}/dt$  slows down drastically, and beyond that point, gas accretion continues and surpasses the core accretion rate. The core mass increases to a value of about  $\sqrt{2}M_{\text{iso}}$  at crossover, when  $M_{\text{core}} = M_{\text{env}}$  (Pollack et al. 1996). This phase of relatively slow accretion rates onto both core and envelope is known as ‘Phase 2’.

### 3. DISK-LIMITED GAS ACCRETION RATES

The epoch of rapid gas accretion in the core-nucleated accretion model generally begins soon after the envelope mass,  $M_{\text{env}}$ , exceeds the core mass,  $M_{\text{core}}$ , as can also be shown by means of simple thermodynamical arguments (D’Angelo et al. 2011). In a proto-solar nebula at  $\sim 5$  AU, this condition typically occurs when the planet mass  $M_p = M_{\text{core}} + M_{\text{env}}$  is between  $\sim 10$  to a few tens of Earth masses. After this point, the planet’s envelope tends to contract very rapidly, limited only by the rate of energy escape at the surface, and a high rate of gas accretion is required to maintain the condition  $R_p = R_{\text{eff}}$ . At or about  $0.25 M_{\text{Jup}}$  this condition can no longer be met, the rate is set by the ability of the protoplanetary disk to deliver gas to the planet, and  $R_p$  contracts well within  $R_{\text{eff}}$ .

There are various regimes of disk-limited gas accretion (see D’Angelo & Lubow 2008). For the purpose of this study, we are mainly interested in the high-mass limit  $R_H \gtrsim H_p$ , where  $R_H = a_p \sqrt[3]{M_p / (3M_*)}$  is the Hill radius of the planet and  $H_p$  is the disk thickness at the planet’s orbital radius,  $a_p$ . In this regime, disk-limited accretion rates can be affected by disk-planet gravitational interactions if tidal torques overcome viscous torques. Assume that the turbulent (kinematic) viscosity of the disk at the orbital distance of the planet is given by  $\nu_t = \alpha_t H_p^2 \Omega_p$ , where  $\Omega_p$  is the local Keplerian rotation frequency of the disk and  $\alpha_t$  is the viscosity parameter. Then tidal torques exerted by the planet on the disk exceed viscous torques exerted by adjacent disk rings on each other if

$$\left(\frac{M_p}{M_*}\right)^2 \gtrsim 3\pi f \alpha_t \left(\frac{H_p}{a_p}\right)^2 \left(\frac{\Delta}{a_p}\right)^3, \quad (7)$$

where  $\Delta = \max(H_p, R_H)$  and  $f$  is a factor of order unity (see, e.g., D’Angelo et al. 2011, and references therein). When the left-hand side of Equation (7) is much greater than the right-hand side, a gap forms in the disk surface density along the planet’s orbital radius.

We estimated disk-limited accretion rates,  $\dot{M}_p$ , using high resolution 3D hydrodynamical simulations of a planet embedded in a protoplanetary disk. We used an approach along the lines of D’Angelo et al. (2003). We considered a disk with a constant aspect ratio of  $H_p/a_p = 0.05$  and with the parameter  $\alpha_t$  ranging from  $4 \times 10^{-4}$  to  $2 \times 10^{-2}$ . The unperturbed surface density

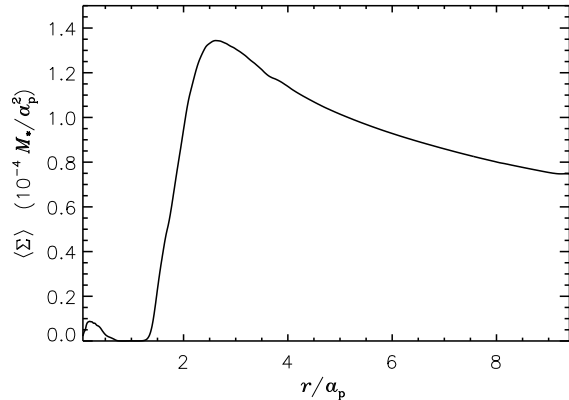


**Figure 1.** Averaged surface density of gas in a disk, as a function of distance from the star, that tidally interacts with a planet with  $M_p = 10^{-2} M_*$ . The orbital radius of the planet is  $a_p$ . The surface density is plotted in scaled units of  $M_*/a_p^2$ . The aspect ratio of the disk is  $H_p/a_p = 0.05$  and the turbulent viscosity parameter is  $\alpha_t = 10^{-2}$ .

of the disk is taken to be a power-law of the distance from the star with exponent  $-1/2$ . The planet is kept on a fixed circular orbit and the continuity and Navier-Stokes equations (written in terms of linear and angular momenta) for the gas are solved in a reference frame co-rotating with the planet.

The disk is assumed to be vertically isothermal and, radially, the temperature drops as the inverse of the distance from the star. At the radial distance  $a_p$ , the temperature is  $T_p = (\mu_d m_H / k_B) H_p^2 \Omega_p^2$ , which is equal to  $53.8 \mu_d$  K at 5 AU from a solar-mass star ( $\mu_d$  indicates the mean molecular weight of the disk’s gas). The relatively simple equation of state adopted here (the pressure  $p \propto T\rho$ , where  $\rho$  is the mass density and the temperature  $T$  is a given function of the orbital distance) allows us to write the fluid equations in a non-dimensional form so that the gas accretion rates can be expressed in terms of  $a_p^2 \Sigma_p \Omega_p$ , where  $\Sigma_p$  is the unperturbed gas surface density of the disk at the planet location (i.e., that the disk would have in the absence of the planet). Furthermore, the planet’s mass enters the calculations only via its ratio to the mass of the star. We considered values of the ratio  $M_p/M_*$  up to 0.02. The planet’s gas accretion rate starts to decline for planet masses greater than the value for which the inequality in Equation (7) is satisfied. This critical mass is larger within more viscous disks. The equation also suggests that there is a dependence on the disk thickness, which, however, was not explored here. We notice that reasonable values of  $H_p/a_p$  for evolved disks, between 1 and 10 AU, range from  $\approx 0.03$  to  $\approx 0.05$  (e.g., D’Angelo & Marzari 2012), affecting the right-hand side of Equation (7) by a factor of less than 3 (for  $R_H > H_p$ ), whereas uncertainties on  $\alpha_t$  are much larger, spanning 2 orders of magnitude or more. An unperturbed surface density with a power index different from that adopted here ( $-1/2$ ) may also affect the accretion rates. We expect these effects to be small, especially when tidal torques exerted by the planet drastically modify the surface density, which is typically the case in the models discussed here.

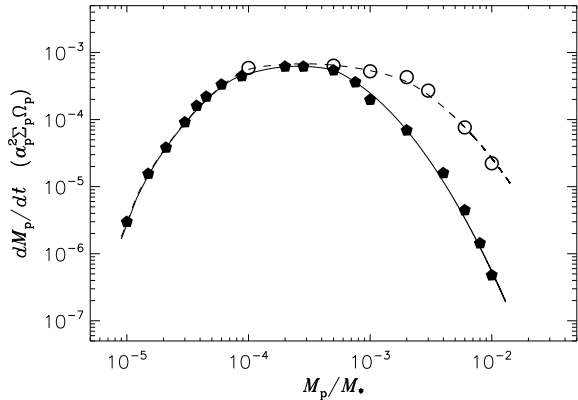


**Figure 2.** Disk-limited gas accretion rates as a function of the planet-to-star mass ratio,  $M_p/M_*$ , for  $H_p/a_p = 0.05$  and for two values of the disk turbulent viscosity parameter:  $\alpha_t = 4 \times 10^{-3}$  and  $10^{-2}$ . Symbols are data obtained from 3D hydrodynamics simulations: filled pentagons/open circles refer to the lower/higher viscosity case. The solid and dashed lines represent results from the fitting procedure outlined in the text. In the units of  $\dot{M}_p$ ,  $\Sigma_p$  represents the unperturbed disk gas surface density and  $\Omega_p$  the Keplerian rotation rate at the planet’s orbital radius,  $a_p$ .

In the calculations, the disk domain extends in radius as close to the star as  $0.1 a_p$  (and  $0.05 a_p$ , in some calculations) and as far as  $9.4 a_p$ . More vigorous perturbations exercised by larger mass planets cause the inner/outer disk radius to decrease/increase with increasing planet-to-star mass ratio. Figure 1 shows the surface density, averaged in azimuth, for a case in which  $M_p = 10^{-2} M_*$  and  $\alpha_t = 10^{-2}$ . Notice that the low densities in the disk inside the orbit of the planet are a consequence of tidal torques and planet accretion (see Lubow & D’Angelo 2006), with possibly some impact from the finite radius of the grid inner boundary ( $0.05 a_p$  in the calculation shown in the figure). The analysis of Lubow & D’Angelo (2006), where applicable, suggests that the effects of the finite inner grid radius are small.

High resolution in and around the planet’s Hill sphere is achieved by means of multiple nested grids (D’Angelo et al. 2002, 2003) centered on the planet’s position. This methodology allows us to solve the fluid equations (locally around the planet), and hence to resolve the accretion flow, on length scales of order  $0.01 R_H$ , or  $\approx 7 R_{Jup}$  at 5 AU.

The gas that orbits the planet deep within its gravitational potential is eventually accreted. We assume that gas can be accreted within a spherical region of radius  $0.1 R_H$  (or  $0.05 R_H$  in some models), centered on the planet. The amount of accreted gas is proportional to the amount of gas available in the region (see D’Angelo & Lubow 2008, and references therein). In these calculations, accreted gas is removed from the computational domain but not added to the mass of the planet in order to achieve a stationary accretion flow (see Lissauer et al. 2009).

We determined an interpolation procedure for the disk-limited gas accretion rates obtained from calculations, by performing piece-wise parabolic fits (in a logarithmic plane) to each  $(\dot{M}_p, M_p/M_*)$  data set, relative to a given value of the turbulent viscosity. Two such fitting

curves are shown in Figure 2 (explicit expressions are provided in Appendix A). Linear interpolations among these curves provide the accretion rate at the desired viscosity parameter,  $\alpha_t$ . In doing so, we derived a function  $\dot{M}_p = \dot{M}_p(M_p, M_*, a_p, \Sigma_p, \alpha_t)$ , which we employ in our planet formation calculations. We recall that  $\Sigma_p$  here represents the disk gas surface density at the planet’s orbital radius, in the absence of the planet. An analytic formula is available for the accretion rate at the low-mass end (D’Angelo & Lubow 2008). However, in the formation calculations the use of these curves is not required until  $M_p$  exceeds  $\approx 0.25 M_{Jup}$ .

During the disk-limited gas accretion phase, the solid accretion rate is arbitrarily limited to a fraction of the value at crossover; the precise value has practically no effect on the results. We don’t expect the core-accretion prescription to be valid at this stage, because most solids in the disk will not be in the form of planetesimals, and we do not have the capability to model giant impacts. As the planet reaches within 2% of the desired final mass (e. g.  $12 M_{Jup}$ ) the gas accretion rate, already quite low, is smoothly reduced to zero.

#### 4. CALCULATIONS AND RESULTS

A recent paper on deuterium burning in objects formed through the core-accretion scenario (Mollière & Mordasini 2012) considered the basic case of a body forming at 5.2 AU in a disk around a  $1 M_\odot$  star with a solid surface density of  $\sigma = 10 \text{ g cm}^{-2}$  and  $T_{\text{neb}} = 150 \text{ K}$ . Their study compared results obtained by varying the following parameters: initial entropy of the object after formation (hot start vs. cold start), helium abundance, metal abundance, initial deuterium mass fraction,  $\sigma$ , which determines the final planet core mass, and maximum gas accretion rate. Their calculations differ from ours in the phase of rapid gas accretion, when disk-limited rates apply. They take that rate to be an arbitrary parameter, while we use the three-dimensional simulations mentioned above (Section 3) to determine it. Here we concentrate on cold-start models and consider a somewhat different set of parameters: stellar mass, formation position of the planet in the disk, solid surface density  $\sigma$ , method of computation of the opacity in the planetary envelope during the formation phase, and protoplanetary disk viscosity parameter  $\alpha_t$ . The planet’s core mass is determined through the calculation itself, and it depends on the first three of these quantities. Note that the final core masses found in our calculations fall in the range  $4.8\text{--}31 M_\oplus$ , while those of Mollière & Mordasini (2012) are higher ( $30\text{--}100 M_\oplus$ ). The formation and evolution are assumed to take place at a fixed orbital radius.

The parameters for the runs are given in Table 1. The columns in the table give, respectively, the run identifier, the mass of the central star in  $M_\odot$ , the distance of the planet from the star, the solid surface density  $\sigma$ , the density  $\rho_{\text{neb}}$  at the surface of the planet during the earlier phases when this surface connects with the disk, the temperature  $T_{\text{neb}}$  at the surface during the same phases, the method of opacity calculation during the formation phase—that is, whether it includes the calculation of grain settling and coagulation (gs) or not (ngs)—, the value of the viscosity parameter  $\alpha_t$  in the disk during the phases of disk-limited gas accretion, and the isola-

**Table 1**  
Input Parameters

Run	M/M <sub>⊙</sub>	Distance (AU)	σ (g cm <sup>-2</sup> )	ρ <sub>neb</sub> (g cm <sup>-3</sup> )	T <sub>neb</sub> (K)	opacity	α <sub>t</sub>	M <sub>iso</sub> (M <sub>⊕</sub> )
1A	1	5.2	10	9 × 10 <sup>-11</sup>	115	gs	1.0 × 10 <sup>-2</sup>	11.6
1B	1	5.2	10	9 × 10 <sup>-11</sup>	115	ngs	1.0 × 10 <sup>-2</sup>	11.6
1C	1	5.2	4	3.7 × 10 <sup>-11</sup>	115	gs	1.0 × 10 <sup>-2</sup>	2.9
2A	2	9.5	4	1.8 × 10 <sup>-11</sup>	125	ngs	1.0 × 10 <sup>-2</sup>	12.6
2B	2	9.5	4	1.8 × 10 <sup>-11</sup>	125	ngs	4.0 × 10 <sup>-3</sup>	12.6
2C	2	9.5	6	2.8 × 10 <sup>-11</sup>	125	ngs	1.0 × 10 <sup>-2</sup>	23.2

tion mass (Equation 6).

Some results for the six runs are presented in Table 2. Each run is given two lines, the first for a final planet mass that burns less than half of its deuterium, the second for a nearby mass that burns more than half. The columns give, respectively, the run identification, the final planet mass in M<sub>Jup</sub>, the total time to reach the final mass (the formation time), the final core mass, the central temperature ( $T_{c,f}$ , at the core/envelope interface) just after formation, the maximum central temperature during D-burning, the central density  $\rho_{c,f}$  just after formation, the planet's radiated luminosity  $L_{c,f}$  just after formation, and the mass fraction of deuterium that remains after 4 Gyr of evolution, in units of the initial D mass fraction of  $4 \times 10^{-5}$ .

#### 4.1. Results for 1 M<sub>⊙</sub>

Run 1A, with standard parameters of 1 M<sub>⊙</sub>, 5.2 AU, and  $\sigma = 10 \text{ g cm}^{-2}$  was originally calculated by Movshovitz et al. (2010) through most of the formation phase, including the detailed calculation of grain opacity (their run  $\sigma 10$ ). Their run, whose characteristics are listed in that paper, ended at the beginning of disk-limited gas accretion, with a core mass of 16.8 M<sub>⊕</sub> and an envelope mass of 56.8 M<sub>⊕</sub> at a total elapsed time of 1 Myr. In this work, the run was continued through the disk-limited phase with  $\alpha_t = 10^{-2}$  (Section 3) up to the mass range required for deuterium burning. The maximum gas accretion rate was  $2.5 \times 10^{-1} \text{ M}_{\oplus} \text{ yr}^{-1}$  at a total planet mass of 96 M<sub>⊕</sub>, declining to  $10^{-2} \text{ M}_{\oplus} \text{ yr}^{-1}$  at 10 M<sub>Jup</sub>. For several different masses in that range, the accretion was terminated, the opacity was reset in the surface layers to the values given by Freedman et al. (2008), and the evolution was followed at constant mass up to Gyr times. The runs were terminated when deuterium burning ceased, and the mass  $M_{50}$ , where 50% of the original deuterium had been burned, was determined. In the Run 1A, the total formation time at  $M_{50}$ , up to termination of accretion, was 1.2 Myr, well within the lifetime of protoplanetary disks.

The planetary luminosity as a function of time for three different final masses in Run 1A is shown in Figure 3, where it is compared with that typically obtained in a 'hot-start' model. In the case of 16 M<sub>Jup</sub>, just after formation the central temperature  $T_{c,f} = 2.8 \times 10^5 \text{ K}$ , too low for substantial burning on a short time scale, even though  $\rho_{c,f} = 80 \text{ g cm}^{-3}$ . Under these conditions the screening correction factor to the nuclear reaction rate is high, about 88. Consequently, deuterium burning can take place at relatively low temperatures compared to those ( $\approx 10^6 \text{ K}$ ) where deuterium burns in solar-mass stars. The central temperature  $T_c$  as a function of time

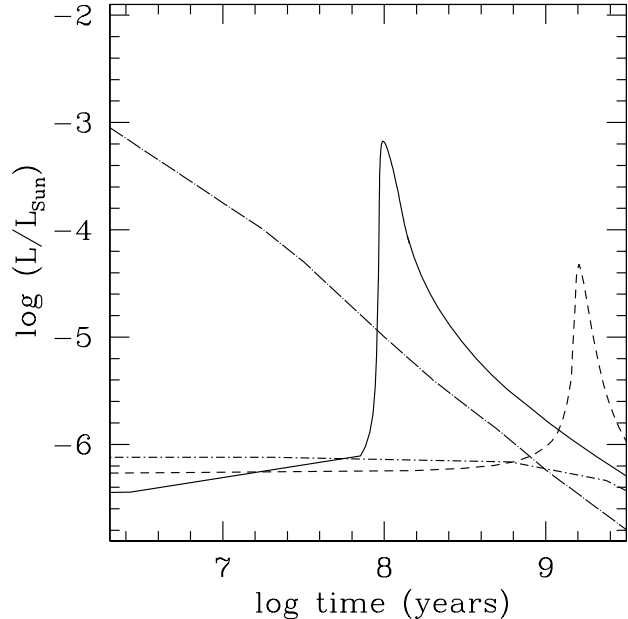


**Figure 3.** Luminosity (in solar units) as a function of time for Run 1A during the post-formation deuterium-burning phase for three different planet masses. *Solid curve*: 16 M<sub>Jup</sub>, *dashed curve*: 12.5 M<sub>Jup</sub>, *short-dash dot curve*: 12 M<sub>Jup</sub>. The *long-dash dot curve* shows the results for a hot-start model of 10 M<sub>Jup</sub> (Baraffe et al. 2003).

(at the core/envelope interface) gradually increases as a result of slow deuterium burning and is accompanied by a slight increase in radius. When  $T_c$  reaches  $3.2 \times 10^5 \text{ K}$ , a rapid increase in burning occurs, leading to a peak in luminosity at about  $10^8$  years. At the peak about 60% of the deuterium has burned, and  $T_c$  is near its maximum of  $5.1 \times 10^5 \text{ K}$ . At the same time the radius has increased from  $7.4 \times 10^9 \text{ cm}$  to  $1.25 \times 10^{10} \text{ cm}$ ; then it contracts again after the luminosity peak. At the end of the evolution essentially all the deuterium has burned. A similar process, involving a rapid increase in deuterium burning in the context of a slowly accreting brown dwarf, was studied by Salpeter (1992); he denotes the event a 'deuterium flash'. The radii for the three masses, as well as for the hot-start case, are shown in Figure 4. The general result that cold-start models result in a radius increase during deuterium burning agrees with the previous results of Mollière & Mordasini (2012).

In the case of 12.5 M<sub>Jup</sub>, right after formation the central temperature is lower, only  $2.6 \times 10^5 \text{ K}$ , with a central density of  $52 \text{ g cm}^{-3}$  and a screening factor of 70. It takes almost  $10^9$  years for rapid deuterium burning to start, at

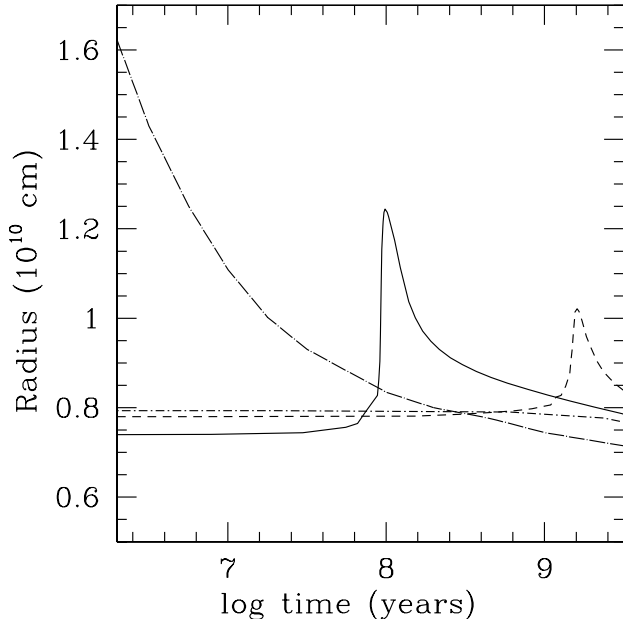


**Figure 4.** Radius (in  $10^{10}$  cm) as a function of time for Run 1A during the post-formation deuterium-burning phase for three different planet masses. *Solid curve:*  $16 M_{\text{Jup}}$ , *dashed curve:*  $12.5 M_{\text{Jup}}$ , *short-dash dot curve:*  $12 M_{\text{Jup}}$ . The *long-dash dot curve* shows the results for a hot-start model of  $10 M_{\text{Jup}}$  (Baraffe et al. 2003).

$T_c = 2.8 \times 10^5$  K, with the burning occurring on a much longer time scale than in the case of  $16 M_{\text{Jup}}$ . Eventually about 98% of the deuterium is burned, and the luminosity peak, which is somewhat lower, is shifted to later times. At the peak, about half of the D has burned, and this point is also close to the maxima in radius and  $T_c$ . In the case of  $12 M_{\text{Jup}}$  only 6% of the deuterium is burned, and no peak in luminosity appears. At  $M_{50}$  itself, the peak involves only a factor 2 increase in luminosity. In the peaks, the total energy  $\int L dt$  is found to agree closely with the total energy available from D-burning, given by the quantity  $Q_{\text{dp}}/m_d \times M_p \times X_d f_d$ , where  $Q_{\text{dp}}$ , the energy production per reaction is expressed in ergs,  $m_d$  is the mass of a deuterium atom,  $M_p$  is the planet mass,  $X_d$  is the initial mass fraction of deuterium, and  $f_d$  is the fraction of the initial D that burned. The total energy is about  $2.5 \times 10^{45}$  ergs for the  $12.5 M_{\text{Jup}}$  case.

Results for two runs whose final masses closely bracket  $M_{50}$  are shown in Table 2. The main result of this case is that  $M_{50} = 12.37 M_{\text{Jup}}$  with a heavy-element core mass of  $16.8 M_{\oplus}$ . By way of comparison, a cold start model with a core, calculated by Mollière & Mordasini (2012) with about the same basic parameters ( $1 M_{\odot}$ ,  $\sigma = 10 \text{ g cm}^{-2}$ ,  $a_p = 5.2 \text{ AU}$ ), with a similar helium mass fraction of 28%, but with some differences in assumptions and computational procedure, gives  $M_{50} = 12.6 M_{\text{Jup}}$ .

The maximum  $T_c$  at the core/envelope interface for  $M_{50}$  in this case is close to  $3.2 \times 10^5$  K, a very sensitive function of mass. Whether significant D-burning occurs depends sensitively on this temperature. If it reaches, say  $2.5 \times 10^5$  K, practically no D is burned for the corresponding mass of  $12.0 M_{\text{Jup}}$ . If it reaches  $4.0 \times 10^5$  K, practically all (98%) of the D is burned for the corresponding mass of  $12.5 M_{\text{Jup}}$ . Once the threshold is reached, en-

ergy deposition from burning increases the temperature, which increases the reaction rate, as it is proportional to  $T^{12}$ . The resulting expansion leads to a near thermal equilibrium, with the energy produced from D-burning matched closely by the total radiated luminosity.

Run 1B differs from 1A only with respect to the calculation of the opacity resulting from grains in the protoplanetary envelope during the formation phase. As mentioned above, in Run 1A this opacity is obtained through detailed consideration of grain settling and coagulation (Movshovitz et al. 2010). In 1B a table of interstellar grain opacities is used, reduced by a factor of about 50. The characteristics of this run, up to a mass of about  $1 M_{\text{Jup}}$ , are very similar to those listed for Run 1sG in Lissauer et al. (2009). The crossover mass is  $16.16 M_{\oplus}$ , the crossover time is 2.31 Myr, and the onset of disk-limited rapid gas accretion occurs at a core mass of  $16.8 M_{\oplus}$  and a time of 2.41 Myr. Note that the evolution time up to this point is 2.4 times longer than in Run 1A. Note also that the core mass is the same as in Run 1A; the substantial difference in opacity, which can be up to two orders of magnitude in certain  $(\rho, T)$  regions, has practically no effect on the core mass.

Here, the disk-limited accretion rates are used to continue the evolution up to the D-burning mass range. The luminosity as a function of time up to the end of accretion is shown in Figure 5. The results for D-burning after that time show that  $M_{50} = 12.20 M_{\text{Jup}}$ , not significantly different from the results of Run 1A. As Table 2 shows,  $T_{c,f}$  in Run 1B, at the same final mass, is slightly higher than that in Run 1A, just after formation. Correspondingly,  $\rho_{c,f}$  is slightly lower. These small differences indicate a slightly higher entropy for 1B after formation, as indicated by the slightly higher luminosity at this point. The increased envelope opacity in 1B as compared with 1A results in slower heat loss and tends to keep internal temperatures higher. However this effect is almost compensated by the fact that the formation time is more than twice as long in 1B. Even the slight increase in  $T_{c,f}$  in 1B as compared with 1A allows  $M_{50}$  to be pushed to a slightly lower mass.

Run 1C differs from Run 1A in that  $\sigma$  is reduced to  $4 \text{ g cm}^{-2}$ , a value only slightly greater than that in a minimum-mass solar nebula (Weidenschilling 1977). Grain settling and coagulation are included in the opacity calculation. The earlier portions of this run, up to the onset of disk-limited gas accretion, are described in Movshovitz et al. (2010), their run  $\sigma 4$ . The time to reach this point, 3.5 Myr, is considerably longer than in Run 1A, first, because the core accretion rate is considerably lower, and second, because the lower isolation mass results in reduced luminosity and reduced gas accretion rate during Phase 2 (Pollack et al. 1996). The crossover mass is  $4.09 M_{\oplus}$ , and the core mass at the time of onset of disk-limited accretion is  $4.74 M_{\oplus}$ .

The calculations were continued up to the point where gas accretion terminated, at which point the core mass was  $4.8 M_{\oplus}$ . The total time to reach  $12 M_{\text{Jup}}$  was about 4.1 Myr, and to  $14 M_{\text{Jup}}$ , about 4.5 Myr. The peak disk-limited accretion rate was  $1.0 \times 10^{-1} M_{\oplus} \text{ yr}^{-1}$  at  $0.3 M_{\text{Jup}}$ , a factor of 2.5 lower than in Run 1A because of the reduction in  $\Sigma_p$  by the same factor. By the time the total mass was  $5 M_{\text{Jup}}$  the rate was down to  $1.8 \times$

$10^{-2} M_{\oplus} \text{ yr}^{-1}$ , and at  $10 M_{\text{Jup}}$  it had further declined to  $4.3 \times 10^{-3} M_{\oplus} \text{ yr}^{-1}$ . Much of the time during the disk-limited accretion phase was spent in accreting the last 1–2  $M_{\text{Jup}}$  to reach the D-burning point. The luminosity as a function of time for this run, up to the end of accretion, is shown in Figure 5.

The luminosity versus time plots for Run 1C during the D-burning phase look similar to those for 1A, except in this case  $M_{50}$  noticeably increases to  $13.55 M_{\text{Jup}}$ . The reduced core mass in 1C ( $4.8 M_{\oplus}$ ) as compared to that in 1A ( $16.8 M_{\oplus}$ ) is clearly associated with the difference, in agreement with the results of [Mollière & Mordasini \(2012\)](#). In our calculations, the core equation of state gives a core radius of  $3.8 \times 10^8$  cm for the Run 1C core of mass  $4.8 M_{\oplus}$  when the total mass is  $12 M_{\text{Jup}}$ . For the core of  $16.8 M_{\oplus}$  in Run 1A, at the same total mass, the radius is  $6.0 \times 10^8$  cm. Thus, at the core boundary, the gravitational potential is more negative, and the gravity is about 40% greater in 1A than in 1C. The calculated values of  $T_{c,f}$  are  $\approx 2.6 \times 10^5$  K and  $\approx 2.1 \times 10^5$  K in Runs 1A and 1C, respectively.

It follows from the equation of hydrostatic equilibrium ([Mollière & Mordasini 2012](#)) that in a convective envelope the adiabatic temperature gradient at the interface should be proportional to the core gravity, so a higher gravity most probably gives a higher temperature. However, this statement is inconclusive. We calculated static models for a planet of  $12 M_{\text{Jup}}$ , all with the envelope entropy of Run 1C, with core masses ranging from 0 to  $15 M_{\oplus}$ . We found practically no difference in  $T_c$  as a function of  $M_{\text{core}}$ , with  $T_c$  decreasing by less than 1% when the core mass increases from 0 to  $15 M_{\oplus}$ .

The real source of the difference in  $T_{c,f}$  between Runs 1A and 1C is the entropy in the envelope. The lower  $T_{c,f}$  and higher  $\rho_{c,f}$  for 1C as compared with 1A indicate a lower entropy, which is consistent with the fact that the luminosity just after formation is lower by more than a factor 2 in 1C (Table 2). The values of entropy just after formation for a planet of  $12 M_{\text{Jup}}$  in Runs 1A and 1C are, respectively, 8.02 and 7.52  $k_B$  per baryon. The entropy is determined through the physical processes that occur during the entire formation phase; for example, the formation time for Run 1C is almost 4 times longer than that for 1A, and the same opacities were used, which suggests a lower entropy. Thus there exists a qualitative understanding of the relation between core mass and  $T_{c,f}$ , but a quantitative theory, apart from the numerical simulations, is quite difficult.

In Run 1C,  $T_{c,f} = 2.1 \times 10^5$  K is the maximum reached for a final mass of  $12 M_{\text{Jup}}$ , and it is insufficient for D-burning. In the case of Run 1A, the corresponding  $T_{c,f}$  is much closer to the threshold required for burning. Thus the planet with the higher  $M_{\text{core}}$  is able to produce significant D-burning at a lower total mass. As Table 2 shows, in the mass range for Run 1C where D-burning begins, just above  $13.5 M_{\text{Jup}}$ ,  $T_{c,f}$  is somewhat less ( $2.3 \times 10^5$  K) than in the corresponding mass range for Run 1A. However, to compensate,  $\rho_{c,f}$  is higher, about  $65 \text{ g cm}^{-3}$ , and the screening factor at the center has increased to 160. Again, the lower entropy at formation for 1C, as compared with 1A, a result of various processes associated with the accretion of core and envelope, leads to a higher  $M_{50}$ .

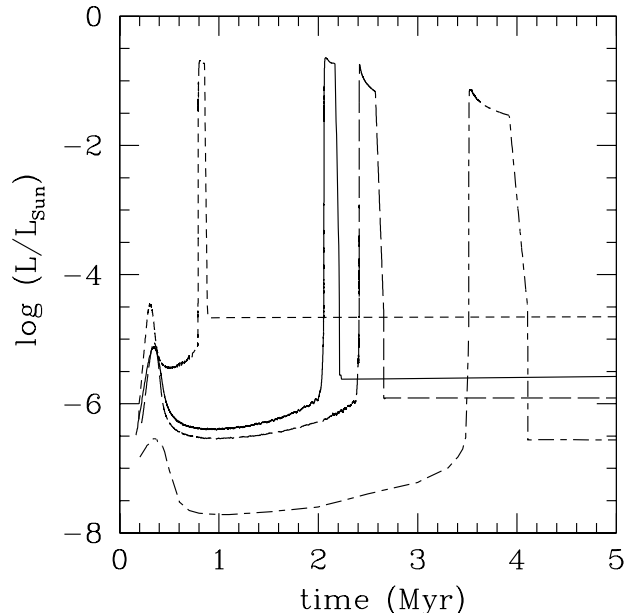


**Figure 5.** Luminosity (in solar units) as a function of time for Run 1B (*long-dashed curve*), Run 1C (*short-dash long-dash curve*), Run 2A (*solid curve*), and Run 2C (*short-dashed curve*) during the formation phase.

#### 4.2. Results for $2 M_{\odot}$

The formation phases of Runs 2A and 2C, for a central star of  $2 M_{\odot}$ , are illustrated in Figure 5, which gives the luminosity as a function of time, and Figure 6, which gives the core mass, envelope mass, and total mass as a function of time. Run 2A differs from 1A in that the planet is placed 9.5 AU away from a star of  $2 M_{\odot}$ , in a disk with  $\sigma = 4 \text{ g cm}^{-2}$ . In a minimum mass solar nebula, scaled to the mass of this star, the corresponding value would be  $2 \text{ g cm}^{-2}$ .

The isolation mass, however is quite similar to that in 1A,  $12.6$  rather than  $11.6 M_{\oplus}$ . The opacity during the formation phase of 2A is taken from a table of interstellar grain opacities, reduced by a factor of 50, as in Run 1B. However, the comparison between 1A and 1B showed that these opacities have little effect on  $M_{50}$ . The formation time is longer in 2A than in 1A because of the longer dynamical time at the larger distance, the reduced solid surface density, and the somewhat higher envelope opacity. However, these effects are partially compensated for by the smaller planetesimal size (50 km in 2A; 100 km in 1A), which increases the capture cross section  $\pi R_{\text{capt}}^2$ , and by the increased gravitational focussing factor  $F_g$  at the larger distance.

The first luminosity peak for Run 2A (Figure 5) occurs at  $t = 3.54 \times 10^5$  yr, with  $\log L/L_{\odot} = -5.14$ , with  $M_{\text{core}} = 9.3 M_{\oplus}$ , with  $M_{\text{env}} = 0.024 M_{\oplus}$ , and with  $\dot{M}_{\text{core}} = 6.67 \times 10^{-5} M_{\odot} \text{ yr}^{-1}$ . This peak corresponds to the maximum in the accretion rate of solids onto the core. The crossover mass (Figure 6) of  $17.6 M_{\oplus}$  is reached in  $2.0 \times 10^6$  years. The second, much higher luminosity peak at  $2.07 \times 10^6$  yr corresponds to the phase of rapid gas accretion up to a final mass of  $15 M_{\text{Jup}}$ . At that time the maximum gas accretion rate is  $2.2 \times 10^{-1} M_{\oplus} \text{ yr}^{-1}$  and  $M_p = 0.47 M_{\text{Jup}}$ . Formation is complete, up to  $15 M_{\text{Jup}}$ ,



**Table 2**  
 Selected Results

Run	$M_{\text{final}}/M_{\text{Jup}}$	$t_{\text{form}}$ (yr)	$M_{\text{core}}/M_{\oplus}$	$T_{\text{c,f}}$ (K)	$T_{\text{max}}$ (K)	$\rho_{\text{c,f}}$ ( $\text{g cm}^{-3}$ )	$\log(L_f/L_{\odot})$	$D_{\text{final}}/D_{\text{init}}$
1A	12.26	$1.19 \times 10^6$	16.8	$2.60 \times 10^5$	$2.60 \times 10^5$	49.7	-6.22	0.895
1A	12.48	$1.20 \times 10^6$	16.8	$2.62 \times 10^5$	$3.54 \times 10^5$	51.4	-6.23	0.164
1B	12.14	$2.67 \times 10^6$	16.8	$2.69 \times 10^5$	$2.69 \times 10^5$	47.0	-5.84	0.860
1B	12.26	$2.68 \times 10^6$	16.8	$2.72 \times 10^5$	$3.18 \times 10^5$	47.7	-5.91	0.328
1C	13.5	$4.37 \times 10^6$	4.83	$2.31 \times 10^5$	$2.31 \times 10^5$	65.1	-6.57	0.938
1C	13.6	$4.39 \times 10^6$	4.83	$2.33 \times 10^5$	$4.27 \times 10^5$	65.9	-6.57	0.292
2A	11.9	$2.14 \times 10^6$	18.7	$2.73 \times 10^5$	$2.81 \times 10^5$	41.4	-5.64	0.767
2A	12.0	$2.14 \times 10^6$	18.7	$2.76 \times 10^5$	$3.06 \times 10^5$	41.8	-5.63	0.435
2B	12.0	$3.23 \times 10^6$	18.8	$2.78 \times 10^5$	$2.87 \times 10^5$	44.6	-5.73	0.582
2B	12.1	$3.26 \times 10^6$	18.8	$2.80 \times 10^5$	$3.28 \times 10^5$	45.1	-5.72	0.320
2C	11.6	$8.75 \times 10^5$	31.0	$3.37 \times 10^5$	$3.46 \times 10^5$	27.9	-4.80	0.670
2C	11.7	$8.75 \times 10^5$	31.0	$3.39 \times 10^5$	$3.56 \times 10^5$	28.3	-4.80	0.390

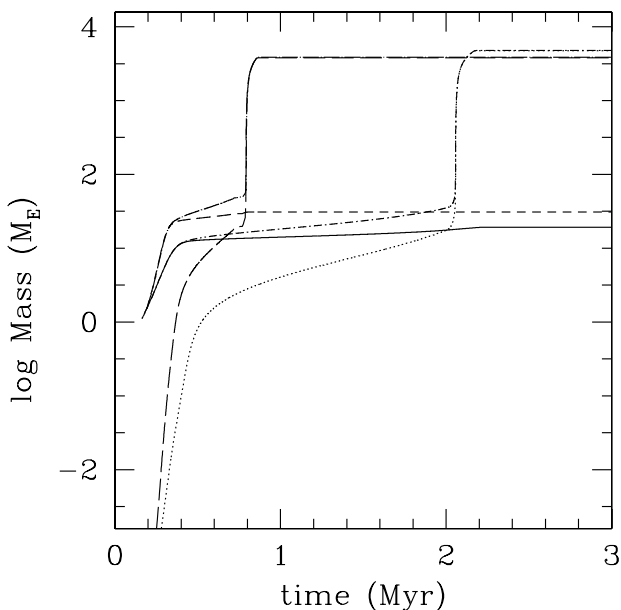


**Figure 6.** Planet mass (in  $M_{\oplus}$ ) as a function of time for Run 2A and Run 2C during the formation phase. The final masses are  $15 M_{\text{Jup}}$  and  $12 M_{\text{Jup}}$ , respectively. For Run 2A, the *solid curve* gives the core mass, the *dotted curve* the envelope mass, and the *short-dash dot curve* the total mass. For Run 2C, the *short-dashed curve* gives the core mass, the *long-dashed curve* the envelope mass, and the *long-dash dot curve* the total mass.

in  $2.2 \times 10^6$  yr. The final  $M_{\text{core}} = 18.7 M_{\oplus}$  is slightly higher than in Run 1A.

The luminosity as a function of time during the later deuterium-burning phase is shown for five different final masses in Run 2A in Figure 7. In the cases of 16 and  $15 M_{\text{Jup}}$ , practically all ( $> 99\%$ ) of the deuterium is burned; in the case of  $13.5 M_{\text{Jup}}$ , about 92% is burned; for  $13.0 M_{\text{Jup}}$ , 75% is burned, and for  $12.0 M_{\text{Jup}}$ , just over 50% is burned. Thus the value for  $M_{50} \approx 11.95 M_{\text{Jup}}$  is very close to the values obtained for Runs 1A/1B despite substantial differences in assumptions and initial conditions. As discussed in the comparison between Runs 1A and 1C, the somewhat larger  $M_{\text{core}}$  in 2A as compared to 1A is the main reason for the slightly lower  $M_{50}$  in 2A. After formation, 2A has a slightly higher  $T_{\text{c,f}}$  than 1A and slightly lower  $\rho_{\text{c,f}}$ , leading to a slightly higher

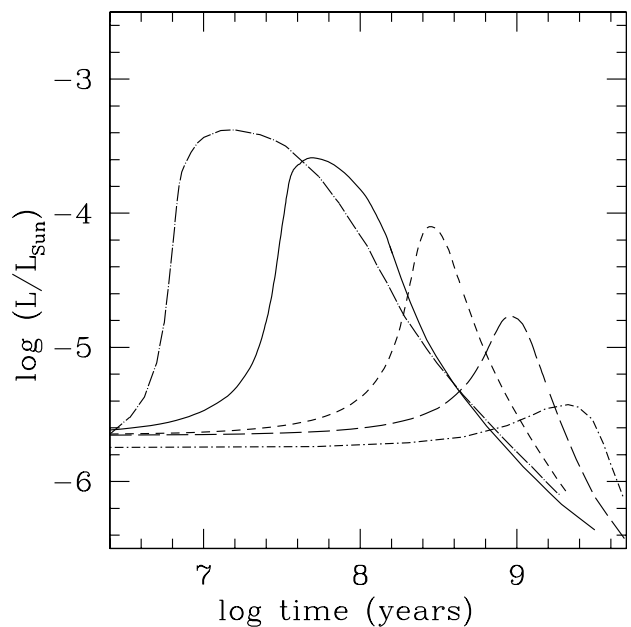


**Figure 7.** Luminosity (in solar units) as a function of time for Run 2A during the post-formation deuterium-burning phase for five different planet masses. *Long-dash dot curve*:  $16 M_{\text{Jup}}$ , *solid curve*:  $15 M_{\text{Jup}}$ , *short-dashed curve*:  $13.5 M_{\text{Jup}}$ , *long-dashed curve*:  $13 M_{\text{Jup}}$ , *short-dash dot curve*:  $12 M_{\text{Jup}}$ .

entropy.

Comparing the luminosity curves for a mass of  $16 M_{\text{Jup}}$  in Figures 3 and 7, they look very different but in fact they are consistent. In Run 2A (Figure 7) the higher  $T_{\text{c,f}}$  (because of the somewhat higher  $M_{\text{core}}$ ) allows D-burning to start earlier than in Run 1A, and the value of  $L$  at the starting point is a factor of 4 higher. In fact the full widths of the two curves are quite similar, the peak values agree to better than a factor 2, and the integrated luminosities over time of the two curves agree to within 10%.

Run 2B has exactly the same parameters as 2A except that  $\alpha_t$  is reduced by a factor 2.5, which affects the gas accretion rates during the disk-limited phase. Thus the formation time in 2B turns out to be a factor of 1.5 longer at  $3.2 \times 10^6$  years, but still within the range of observed disk lifetimes. Table 2 shows that for final mass  $12 M_{\text{Jup}}$

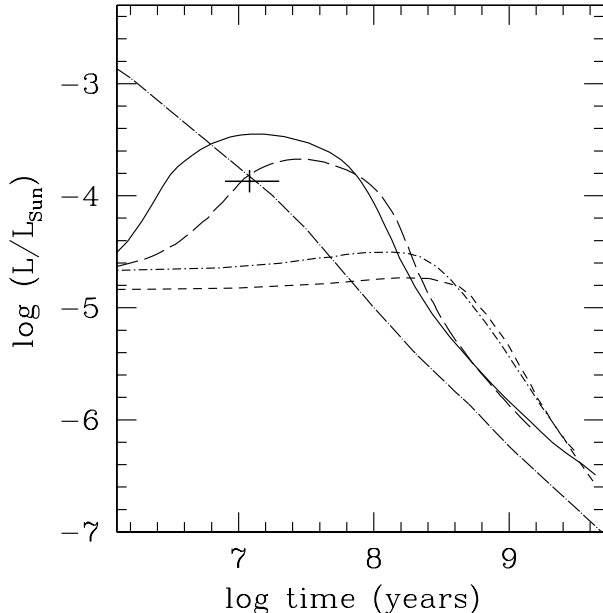


**Figure 8.** Luminosity (in solar units) as a function of time for Run 2C during the post-formation deuterium-burning phase for four different planet masses. *Solid curve:* 15  $M_{\text{Jup}}$ , *long-dashed curve:* 13.7  $M_{\text{Jup}}$ , *short-dash dot curve:* 12  $M_{\text{Jup}}$ , *short-dash curve:* 11.7  $M_{\text{Jup}}$ . The *long-dash dot curve* shows a hot-start model for 10  $M_{\text{Jup}}$  (Baraffe et al. 2003). The cross gives the position and error bars for the companion to Beta Pic (Bonnetfey et al. 2013).

the fractions of deuterium burned are in agreement for runs 2A and 2B, within the uncertainties of the calculations. Thus  $\alpha_t$  has practically no effect on  $M_{50}$  in this case. Run 2B has a slightly lower entropy than 2A at 12  $M_{\text{Jup}}$ , 8.2  $k_B$  per baryon versus 8.25, and therefore a slightly higher  $M_{50}$ . Thus it appears that the longer time during disk-limited accretion in Run 2B has only a weak effect on both  $M_{50}$  and the entropy, at the same  $M_{\text{core}}$ .

Run 2C has the same parameters as 2A except that the solid surface density  $\sigma$  is increased by a factor 1.5 to 6  $\text{g cm}^{-2}$ . The first luminosity peak (Figure 5) occurs at  $t = 3.07 \times 10^5$  years with  $\log L/L_{\odot} = -4.45$  at  $M_{\text{core}} = 15.6 M_{\oplus}$ . The crossover mass (Figure 6) is reached at  $t = 7.88 \times 10^5$  yr with a value of 30.7  $M_{\oplus}$ . The maximum luminosity in the second peak is above  $\log L/L_{\odot} = -1$ , at  $t = 7.915 \times 10^5$  years and a total mass of 0.62  $M_{\text{Jup}}$ . The higher  $\sigma$  with respect to Run 2A results in a markedly higher  $M_{\text{core}} = 31 M_{\oplus}$  and a markedly shorter formation time ( $8.75 \times 10^5$  yr at  $M_{50}$ ). Despite these relatively large differences, the value for  $M_{50}$  in 2C is only 2.5% smaller than in 2A. At the end of the formation phase, central temperatures are higher and central densities are lower in 2C as compared with 2A. Also, the screening factor is only 14 in 2C compared with 41 for 2A. The entropy at formation, for a final mass of 12  $M_{\text{Jup}}$ , is higher in 2C, 9.08  $k_B$ /baryon as compared with 8.25, corresponding to a higher luminosity at that point. The slope in the ( $M_{\text{core}}, M_{50}$ ) diagram between  $M_{\text{core}} = 18.7$  and 31  $M_{\oplus}$  is -0.024, a result which differs somewhat from that of Mollière & Mordasini (2012). They obtain a slope (in the same units) of -0.01, although for a different core mass range, 30 to 100  $M_{\oplus}$ .

Plots of luminosity versus time are shown in Figure 8 for several different masses in Run 2C. As in Figure 7 the higher masses give higher peak luminosity at earlier times than the lower masses, and at  $M_{50}$  there is only a very small peak. The  $L(t)$  curve for 15  $M_{\text{Jup}}$  starts at a higher value and reaches a maximum sooner than for the same mass in Run 2A, because of the higher internal temperature, but the value of  $\log L$  at the peak is about the same. At 13.7 and 15  $M_{\text{Jup}}$  practically all of the initial D is burned. At 12  $M_{\text{Jup}}$ , 72% is burned, while at 11.7  $M_{\text{Jup}}$ , which is very close to  $M_{50}$ , 61% is burned.

Plots of  $T_c$  versus time, during the deuterium-burning phases, are shown for masses 12 and 15  $M_{\text{Jup}}$  in Figure 9, where they are compared with the results from Run 2A. The plot shows the effect of varying the core mass at fixed total mass, and of varying the total mass at fixed core mass. For example, for Run 2A at 15  $M_{\text{Jup}}$  the maximum  $T_c$  is  $4.6 \times 10^5$  K, while for 12  $M_{\text{Jup}}$  it is only  $3.06 \times 10^5$  K and is reached at a much later time. The vertical portions of these curves show the effect of rapid gas accretion from about 1  $M_{\text{Jup}}$  to the final mass of either 12 or 15  $M_{\text{Jup}}$ . The two nearly horizontal curves are for a total mass of 12  $M_{\text{Jup}}$  and core masses of 18.7 (lower; Run 2A) and 31  $M_{\oplus}$  (upper; Run 2C). The higher core mass results in a higher temperature by a factor of about 1.3. In the case of the 31  $M_{\oplus}$  core, about 75% of the deuterium is burned; in the 18.7  $M_{\oplus}$  core, a little over 50%. Note that the D-burning occurs late in the evolution, where small peaks in the temperature are seen. The remaining two curves correspond to a total mass of 15  $M_{\text{Jup}}$ , with the same two core masses just mentioned. The D-burning occurs earlier than in the case of the lower total mass, and the higher core mass again gives a higher maximum  $T_c$ . In both cases for 15  $M_{\text{Jup}}$  practically all the D is burned, and the residual mass fraction is smaller ( $8.9 \times 10^{-11}$ ) for the higher core mass as compared to the lower ( $2.6 \times 10^{-9}$ ).

In Run 2C with 15  $M_{\text{Jup}}$ ,  $T_c$  goes up to about  $5 \times 10^5$  K and there are actually two minor peaks. Figure 10 illustrates in more detail how various quantities vary during this phase. In this case, with a high  $T_{c,f}$ , nuclear burning starts very early. During most of the phase, the object is not in thermal equilibrium. The first maximum in  $T_c$  occurs when about 25% of the D has burned, close to the time of the maximum in the nuclear burning luminosity  $L_{\text{nuc}}$ . Here  $L_{\text{nuc}}$  is well above the radiated luminosity  $L$ , and the extra power goes into expansion, resulting in slight cooling of the interior. When half the deuterium has burned ( $1.3 \times 10^7$  yr), there is a maximum in luminosity and radius, corresponding to the slight minimum in  $T_c$ . Then contraction along with a slow decrease in nuclear burning leads to slight heating, and the second maximum occurs when 98% of the D has burned. This maximum corresponds to the time when  $L_{\text{nuc}}$  starts to drop rapidly and to fall well below  $L$ . Beyond that point, even though contraction is occurring, there is insufficient burning to maintain the high temperature, and the object enters its final cooling phase. In contrast, in the case of 12  $M_{\text{Jup}}$ , the main D-burning in Run 2C takes place at practically constant  $T_c$ , radius, and  $L$ , with a slight maximum in  $T_c$  of  $3.67 \times 10^5$  K at about  $10^8$  yr. In this case the configuration is close to thermal equilibrium through most of the D-burning phase.

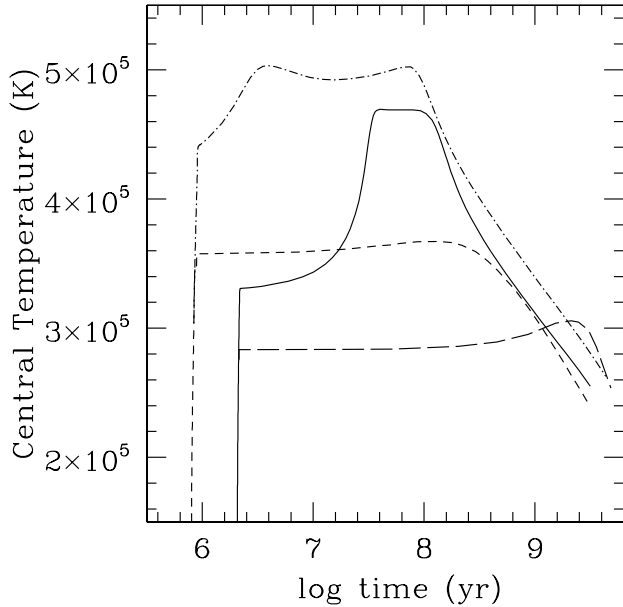


**Figure 9.** Central temperature  $T_c$  (at the core/envelope interface) as a function of time for four cases. *Solid curve*: Run 2A ( $15 M_{\text{Jup}}$ ), *long-dashed curve*: Run 2A ( $12 M_{\text{Jup}}$ ), *dash-dot curve*: Run 2C ( $15 M_{\text{Jup}}$ ), *short-dashed curve*: Run 2C ( $12 M_{\text{Jup}}$ ). The phases of rapid gas accretion and final phases of constant mass with deuterium burning are shown. Core masses for Runs 2A and 2C are  $18.7$  and  $31 M_{\oplus}$ , respectively.

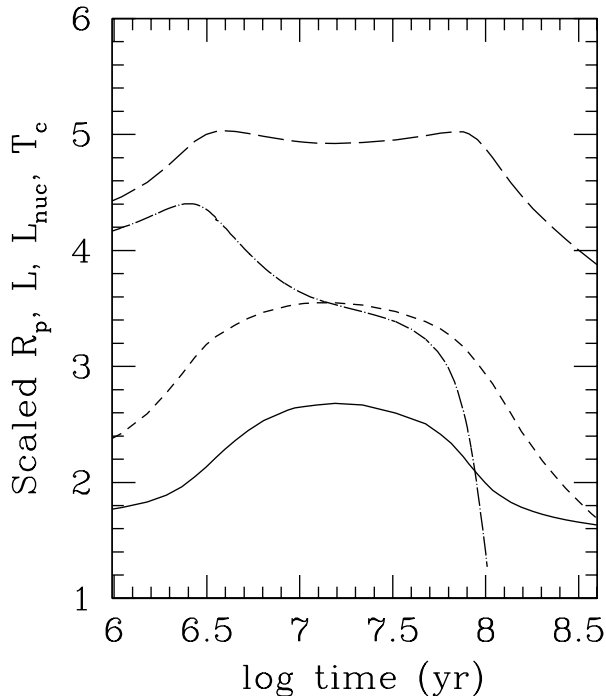


**Figure 10.** Detail of the deuterium-burning phase for Run 2C,  $15 M_{\text{Jup}}$ . *Solid curve*: outer radius  $R_p$  as a function of time, in units of  $5 \times 10^9$  cm; *long-dashed curve*: central temperature  $T_c$ , at the core/envelope interface, as a function of time, in units of  $10^5$  K; *dash-dot curve*: nuclear luminosity as a function of time in units of  $\log(L_{\text{nuc}}/L_{\odot}) + 7$ ; *short-dashed curve*: radiated luminosity  $L$  as a function of time, in the same units as  $L_{\text{nuc}}$ .

#### 4.3. Comparison with beta Pictoris b

The cross in Figure 8 gives the approximate location of the directly imaged companion (Lagrange et al. 2009) to the well-known star Beta Pictoris. That star, according to <http://exoplanet.eu>, has a mass of about  $1.8 M_{\odot}$  and an age of  $12 (+8, -4)$  Myr. The planet is located between 8 and 15 AU from the star (Lagrange et al. 2010); thus an approximate comparison can be made with these calculations. Beta Pic b’s position in the  $(\log L, t)$  diagram is plotted in Marois et al. (2010) where it is shown to fall on a theoretical track with mass  $10 M_{\text{Jup}}$  as calculated from a ‘hot start’ by Baraffe et al. (2003). In <http://exoplanet.eu> that mass is given as  $8 (+5, -2) M_{\text{Jup}}$ . The surface temperature  $T_{\text{eff}}$  has been estimated from observed near infrared colors (Bonnetfoy et al. 2011; Quanz et al. 2010) at 1700 K, with considerable uncertainty ( $\approx 300$  K). Further infrared and astrometric observations (Bonnetfoy et al. 2013) are essentially in agreement, giving  $\log(L/L_{\odot}) = -3.87 \pm 0.08$ ,  $T_{\text{eff}} = 1700 \pm 100$  K,  $a_p = 8 - 10$  AU, and ‘hot-start’ masses in the range  $7-13 M_{\text{Jup}}$ . The bolometric luminosity found by Marleau & Cumming (2013) is in agreement with the above value, and they find ‘hot-start’ masses in the range  $7-12 M_{\text{Jup}}$ .

In our ‘cold-start’ calculations the track for Run 2C,  $13.7 M_{\text{Jup}}$ , passes close to the object in the  $(\log L, t)$  diagram, and the calculations give  $T_{\text{eff}} = 1627$  K at an age of 12 Myr. Our mass  $10 M_{\text{Jup}}$  cannot possibly provide a fit. The ‘hot-start’ models thus would show that the object is a planet, as defined by an object with mass not high enough to burn deuterium. However this particular ‘cold-start’ model indicates that beta Pictoris b is presently burning deuterium, which, according to the same definition, would classify it as a brown dwarf. As mentioned in Section 1, this definition is not universally agreed upon; an alternative definition, based on the minimum in the mass distribution of low-mass companions, observed within several AU of sunlike stars, places the limit at  $\approx 25 M_{\text{Jup}}$ . In this case Beta Pic b would still be a planet. Note that in the ‘cold-start’ calculations, the fit at  $13.7 M_{\text{Jup}}$  with an assumed  $\sigma = 6 \text{ g cm}^{-2}$  is not unique; the companion could also be fit at  $\sigma = 4 \text{ g cm}^{-2}$  at a slightly higher mass, about  $15.6 M_{\text{Jup}}$ . Furthermore, these masses are uncertain and will probably change when the calculations are redone in the future with more detailed model atmospheres. Nevertheless, as such they are marginally consistent with the upper limits to the mass of Beta Pic b derived from radial velocity measurements (Lagrange et al. 2012). For a planet at 9 AU the limit is  $12 M_{\text{Jup}}$ ; at 10 AU it is  $15.4 M_{\text{Jup}}$ .

We note also that the luminosity curve for  $11.7 M_{\text{Jup}}$  in Figure 8 agrees well with the observed luminosity of the directly imaged planet HR 8799 c at the stellar age ( $\approx 6 \times 10^7$  years). The observed value is given by Marley et al. (2012) as  $\log L/L_{\odot} = -4.9 \pm 0.1$ . The agreement of course requires a core mass of  $\approx 30 M_{\oplus}$ . A hot-start model of about  $10 M_{\text{Jup}}$  without a core also agrees. However we do not make a detailed comparison with HR 8799 c, because the metallicity of the star is low ( $[\text{Fe}/\text{H}] = -0.47$ ) and the planet orbits at 43 AU, making it highly debatable whether it could have formed by core-nucleated accretion.

**Table 3**  
Summary

Run	M/M <sub>⊙</sub>	Distance (AU)	σ (g cm <sup>-2</sup> )	M <sub>core</sub> (M <sub>⊕</sub> )	M <sub>50</sub> (M <sub>Jup</sub> )
1A	1	5.2	10	16.8	12.37
1B	1	5.2	10	16.8	12.20
1C	1	5.2	4	4.83	13.55
2A	2	9.5	4	18.7	11.95
2B	2	9.5	4	18.8	12.05
2C	2	9.5	6	31.0	11.65

## 5. SUMMARY AND CONCLUSIONS

We investigate the boundary between brown dwarfs and giant planets, according to the definition that brown dwarfs can burn the deuterium that is present when they form, and giant planets cannot. The main parameters and the results for  $M_{50}$ , the boundary mass at which half of the original deuterium is burned after 4 Gyr, are summarized in Table 3. The columns give, respectively, the run identification, the stellar mass in  $M_{\odot}$ ,  $a_p$ , the initial disk solid surface density  $\sigma$  at  $a_p$ , the resulting  $M_{\text{core}}$ , and  $M_{50}$ . The main cases considered involve a planet/brown dwarf at 5.2 AU around a solar-mass star, and a planet/brown dwarf at 9.5 AU around a star of  $2 M_{\odot}$ . The table shows that there is only a small variation in the values of  $M_{50}$ , which, however, correlate with the core mass in the sense that the smaller the core mass, the higher the value of  $M_{50}$ .

The calculations, taken as a whole, indicate that the envelope entropy, which is a function of initial conditions and which is closely related to the core mass through the accretion processes during the formation phase, is an important factor in determining  $M_{50}$ . However, certain physical processes during formation are shown to have only a small effect. Run 1B has the same parameters as Run 1A except that the dust opacity during the formation phase is higher by a factor that ranges from 2 to 100, depending on the depth in the envelope. This difference has a negligible effect on  $M_{50}$ . Run 2B has the same parameters as 2A except that the disk viscosity during the phase of disk-limited gas accretion is lower by a factor 2.5. This difference also has a negligible effect on  $M_{50}$ . However the disk viscosity is important in another respect. If it is significantly lower than the range presented here ( $\alpha_t \approx 10^{-2}$ ), then there will not be time to accrete a planet with mass necessary to burn deuterium during the lifetime of the disk. The gas accretion rate onto a planet of  $4 M_{\text{Jup}}$  around a star of  $2 M_{\odot}$ , in a disk with  $\alpha_t = 4 \times 10^{-4}$ , is reduced by a factor 400 compared with a disk with  $\alpha_t = 4 \times 10^{-3}$  (Lissauer et al. 2009), corresponding to less than a Jupiter mass in a million years for the initial conditions of Run 2B (formation time about 3 Myr). Of course the minimum viscosity required to build a planet up to about  $12 M_{\text{Jup}}$  will depend on parameters such as  $\sigma$  and  $a_p$ . This question is discussed in more detail in Appendix A.

Core accretion models, in the cold-start case, are known to have low entropy compared with hot-start models. In Marley et al. (2007) the entropy just after formation for  $10 M_{\text{Jup}}$  was found to be  $8.2 k_B$  per baryon for  $M_{\text{core}} = 16.8 M_{\oplus}$ . The corresponding luminosity at ages of  $10^7$  to  $10^8$  years was about  $2 \times 10^{-6} L_{\odot}$ , certainly

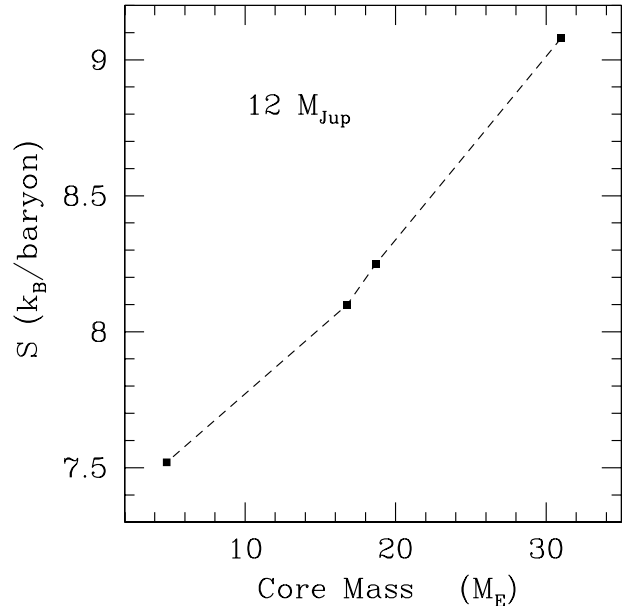


**Figure 11.** The entropy in the interior of planets of total mass  $12 M_{\text{Jup}}$ , immediately after formation, is plotted against their core masses, in  $M_{\oplus}$ . The points plotted, from top to bottom, are from Runs 2C, 2A, 1B, and 1C.

fainter than observed values for directly imaged planets. In this mass range, for the given core mass, the entropy is very insensitive to the planet's total mass, as shown in that paper and confirmed by the present results. However our calculations show that the entropy is quite sensitive to the core mass, as illustrated in Figure 11 (a similar effect has been found independently by Mordasini (2013) for  $M_{\text{core}} > 20 M_{\oplus}$ ). The points shown are all calculated with the same total mass and the same disk viscosity. All used the reduced interstellar grain opacity, except for the point at  $M_{\text{core}} = 4.8 M_{\oplus}$ , for which the grain-settling opacities were used (if the interstellar opacities had been used, the formation time would have been considerably longer). However the comparison between Runs 1A and 1B, which looked at the effect of changing the opacities, showed that the difference in entropy was less than  $0.1 k_B$  per baryon at the same total mass. The effect on the entropy of changing the viscosity (Runs 2A and 2B) was even smaller. Physical effects that do affect the entropy include the planetesimal accretion rate and the rate of contraction of the envelope, both of which affect the internal heating of the envelope. Thus the luminosities of newly formed massive planets, depending on formation conditions, can vary by up to two orders of magnitude.

**Table 4**  
Data for Figure 11

Run	$M_{\text{final}}/M_{\text{Jup}}$	$t_{\text{form}}$ (yr)	$M_{\text{core}}/M_{\oplus}$	$T_{\text{c,f}}$ (K)	$T_{\text{max}}$ (K)	$\rho_{\text{c,f}}$ ( $\text{g cm}^{-3}$ )	$\log(L_{\text{f}}/L_{\odot})$	$D_{\text{final}}/D_{\text{init}}$
2C	12.0	$8.83 \times 10^5$	31.0	$3.48 \times 10^5$	$3.67 \times 10^5$	29.6	-4.80	0.278
2A	12.0	$2.14 \times 10^6$	18.7	$2.76 \times 10^5$	$3.06 \times 10^5$	41.8	-5.63	0.435
1B	12.0	$2.66 \times 10^6$	16.8	$2.66 \times 10^5$	$2.66 \times 10^5$	46.1	-5.91	0.930
1C	12.0	$4.10 \times 10^6$	4.80	$2.08 \times 10^5$	$2.08 \times 10^5$	54.0	-6.56	1.000

Information on the runs whose entropies are plotted in the figure is given in Table 4. The table is in the same format as Table 2 and gives the runs in order of decreasing entropy. Clearly, for this set of models, a lower entropy is associated with a longer formation time. The luminosity plots for these four cases in Figure 5 illustrate the same effect.

The combination of  $M_*$ ,  $a_p$ , and  $\sigma$  determines the isolation mass, and thereby the ultimate core mass, which turns out to be a key factor in determining the entropy of the planet at formation. Higher entropy, in particular the higher temperature, favors more rapid nuclear burning, so the higher entropy runs result in lower values of  $M_{50}$ . Nevertheless, the range of initial conditions explored here, which is considerable, produces only a small range in  $M_{50}$ , about 11.6–13.6  $M_{\text{Jup}}$ , in agreement with previous independent calculations. We can further conclude, that for cold-start core-accretion models that do burn deuterium, the tracks in the luminosity versus time diagram can potentially provide agreement with the

properties of directly-imaged low-mass stellar companions.

Primary funding for this project was provided by the NASA Origins of Solar Systems Program grant NNX11AK54G (P. B., G. D., J. L.). G.D. acknowledges additional support from NASA grant NNX11AD20G. P. B. acknowledges additional support from NSF grant AST0908807. D. S. is supported in part by NASA grants NNH11AQ54I and NNH12AT89I. The authors are indebted to Gilles Chabrier for the use of his nuclear screening factors. The 3D hydrodynamical simulations reported in this work were performed using resources provided by the NASA High-End Computing (HEC) Program through the NASA Advanced Supercomputing (NAS) Division at Ames Research Center. G.D. thanks Los Alamos National Laboratory for its hospitality. The authors thank the referee Dr Christoph Mordasini for a detailed and constructive review.

## APPENDIX

### A. ANALYTIC APPROXIMATIONS OF THE DISK-LIMITED GAS ACCRETION RATES

In this section, we provide analytic approximations for the gas accretion rate in the regime where this rate is limited by the ability of the disk to transfer gas to the planet. In the calculations, we used piece-wise functions obtained by fitting the data from the 3D hydrodynamical calculations (see Section 3), for various values of the turbulent viscosity parameter,  $\alpha_t$ , which quantifies the kinematic viscosity of the disk at the radial location of the planet,  $\nu_t = \alpha_t H_p^2 \Omega_p$ . We recall that the hydrodynamical calculations used an aspect ratio  $H_p/a_p = 0.05$ , which is a reasonable value in evolved disks between 5 and 10 AU (e.g., D’Angelo & Marzari 2012, and references therein).

We fitted  $(\log \dot{M}_p, \log M_p)$  data using multiple second-order polynomials, which were then smoothly joined in overlapping regions. Since this procedure is somewhat cumbersome, here we provide simpler analytic approximations derived from data in the range of  $M_p/M_*$  from  $10^{-4}$  to  $10^{-2}$ . In the calculations, as explained in Section 3, disk-limited accretion sets in when  $M_p \gtrsim 0.25 M_{\text{Jup}}$ .

Let us introduce the four functions

$$f_1(q) = a_0 + a_1 \log q + a_2 (\log q)^2 \quad (\text{A1})$$

$$f_2(q) = b_0 + b_1 \log q + b_2 (\log q)^2 \quad (\text{A2})$$

$$f_3(q) = c_0 + c_1 \log q + c_2 (\log q)^2 \quad (\text{A3})$$

$$f_4(q) = d_0 + d_1 \log q + d_2 (\log q)^2, \quad (\text{A4})$$

where  $q = M_p/M_*$  and all logarithms are in base 10. The coefficients  $a_i, b_i, c_i$ , and  $d_i$  are given in Table A1. For  $\alpha_t = 10^{-2}$ , the following analytic approximation for the disk-limited gas accretion rate, in units of  $a_p^2 \Sigma_p \Omega_p$ , may be used:

$$\log \dot{M}_p = \begin{cases} f_1(q) & \text{if } q < 0.001197 \\ f_2(q) & \text{otherwise.} \end{cases} \quad (\text{A5})$$

For  $\alpha_t = 4 \times 10^{-3}$ , the following analytic approximation may be applied

$$\log \dot{M}_p = \min [f_3(q), f_4(q)]. \quad (\text{A6})$$

The fitting functions are shown in the upper panel of Figure A1, along with the data obtained from the 3D hydrodynamical calculations.

In the range of the turbulent parameter  $\alpha_t$  that we explored ( $4 \times 10^{-4} \leq \alpha_t \leq 0.02$ ), the maximum of  $\dot{M}_p$  occurs at a ratio  $M_p/M_*$  similar (within a factor of  $\approx 2$ ) to the square root of the right-hand side of Equation (7), i.e., before gas

**Table A1**  
Coefficients in Equations (A1)–(A4)

	$i = 0$	$i = 1$	$i = 2$
$a_i$	−6.8345179	−2.5152600	−0.354296
$b_i$	−12.471200	−6.3732500	−1.014440
$c_i$	−11.429400	−5.0171300	−0.697484
$d_i$	−17.819292	−8.5200885	−1.172181

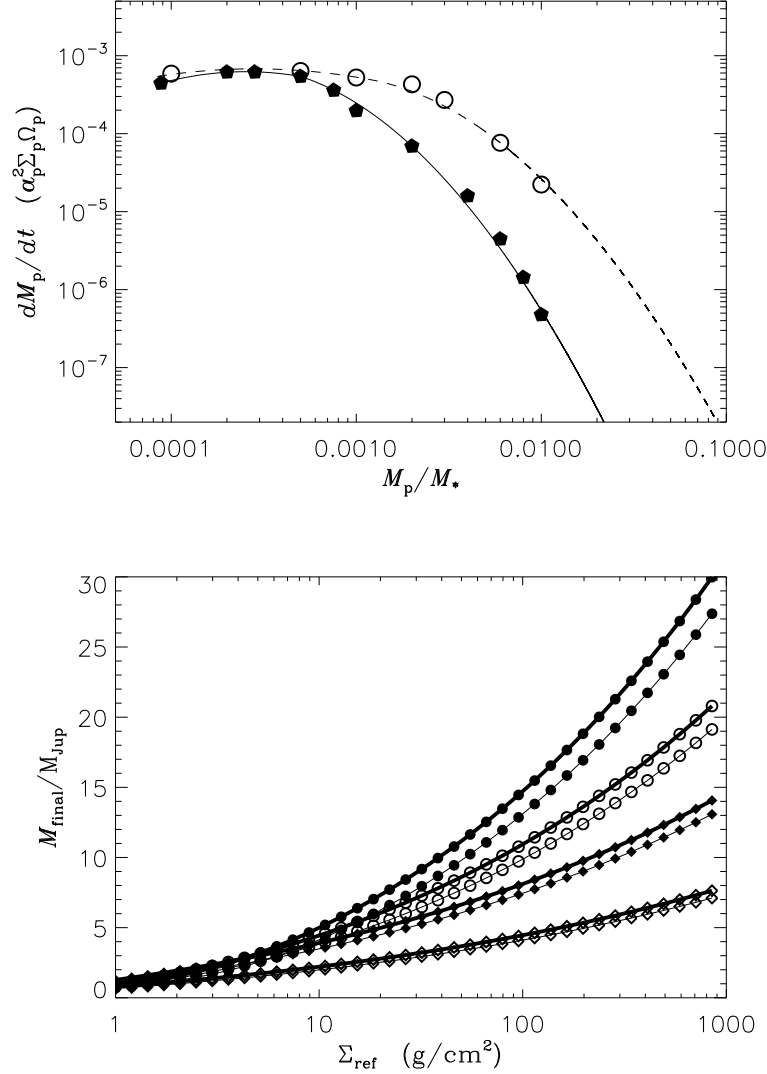


**Figure A1.** *Upper panel:* disk-limited gas accretion rates versus the planet-to-star mass ratio (see also Figure 2). The dashed line is Equation (A5), the solid line is Equation (A6), and the symbols represent the simulations' data for the disk turbulent parameter  $\alpha_t = 10^{-2}$  (open circles) and  $4 \times 10^{-3}$  (filled pentagons). *Lower panel:* final mass of a planet accreting at a disk-limited gas accretion rate in various situations:  $\alpha_t = 4 \times 10^{-3}$  (diamonds),  $\alpha_t = 10^{-2}$  (circles),  $a_p = 5.2$  AU (thin lines),  $a_p = 9.5$  AU (thick lines),  $M_* = 1 M_\odot$  (open symbols), and  $M_* = 2 M_\odot$  (filled symbols). See text for further details.

begins to be depleted significantly because of the formation of the density gap. The maximum of  $\dot{M}_p$  can be compared to the (steady state) accretion rate through the disk in absence of the planet,  $3\pi\nu_t\Sigma_p$  (Lynden-Bell & Pringle 1974), at the radial location of the planet. In units of  $a_p^2\Sigma_p\Omega_p$ , this accretion rate can be written as  $3\pi\alpha_t(H_p/a_p)^2$ , giving  $\approx 10^{-4}$  and  $2.4 \times 10^{-4}$  for  $\alpha_t = 0.004$  and 0.01, respectively. As can be seen in Figure A1, these disk accretion rates are smaller than the maximum of  $\dot{M}_p$ . However, it should be noted that the tidal perturbation of the planet can modify

the accretion rate through the disk (Lubow & D’Angelo 2006).

Equations (A5) and (A6) can be integrated to find the final (asymptotic) mass of a planet,  $M_{\text{final}}$ , that accretes gas at a disk-limited gas accretion rate. We solved numerically the differential equation

$$\dot{M}_p = F(M_p, M_*, a_p, \Sigma_p, \alpha_t) \quad (\text{A7})$$

for  $M_p$ , using an adaptive Adams-Bashforth-Moulton method of variable order with adaptive step-size and error control (available through the SLATEC Common Mathematical Library). Notice from Equation (A7) that, although the dependence of  $\dot{M}_p$  on  $M_*$ ,  $a_p$ , and  $\Sigma_p$  is trivial, the dependence of  $M_p(t)$  on those three quantities is not!

During the integration of Equation (A7), we assumed that  $M_*$ ,  $a_p$ , and  $\alpha_t$  are constants. In order to mimic the viscous evolution of the (unperturbed) gas surface density at the radial position of the planet,  $\Sigma_p$ , we applied the solution of Lynden-Bell & Pringle (1974) for a disk with no central couple. Using the same notations and indicating with  $R_1$  the initial standard deviation of the (gaussian) surface density distribution and with  $M_1$  the initial disk mass, Lynden-Bell & Pringle (1974) found that  $\nu_t/R_1^2 = (2/3)\dot{M}_*/M_1$  (where  $\dot{M}_*$  is the initial accretion rate on the star). Introducing the non-dimensional ‘viscous’ time<sup>†</sup>  $t_{\text{vis}} = 6(\nu_t/R_1^2)t + 1$ , which can be written as  $t_{\text{vis}} = 4(\dot{M}_*/M_1)t + 1$ , the surface density evolution can be approximated by

$$\Sigma_p = \Sigma_{\text{ref}} t_{\text{vis}}^{-5/4}, \quad (\text{A8})$$

where  $\Sigma_{\text{ref}}$  is a parameter and which represents the behavior of the Lynden-Bell & Pringle solution for  $t_{\text{vis}} \gg 1$ . We assumed that  $\dot{M}_*/M_1$  is  $\approx 10^{-6} \text{ yr}^{-1}$ . According to the equation above, the surface density ratio  $\Sigma_p/\Sigma_{\text{ref}}$  decreases by more than two orders of magnitude over 10 Myr.

We integrated Equation (A7) for the values of  $M_*$ ,  $a_p$ , and  $\alpha_t$  used in the calculations, applying Equation (A8), and determined  $M_{\text{final}}$  as a function of  $\Sigma_{\text{ref}}$ . The results are shown in the lower panel of Figure A1 (see figure caption for a description of the different curves). The final mass is reached within about 5.5 Myr, when typically  $M_p/\dot{M}_p \sim 100 \text{ Myr}$ . The effect of disk viscosity is evident in this figure. In fact, around a solar mass star, the mass threshold for deuterium burning can only be achieved for  $\alpha_t \gtrsim 10^{-2}$ . Among the varied parameters,  $\alpha_t$  produces the largest differences in  $M_{\text{final}}$ , whereas  $a_p$  produces the smallest. Notice that the values of  $M_{\text{final}}$  shown in the lower panel of Figure A1 should not necessarily agree with those in the D-burning calculations because of the different assumptions made for the nebula evolution. In particular,  $\Sigma_p$  in those calculations was taken as a constant.

<sup>†</sup> Notice that the power of  $R_1$ , in the definition of Lynden-Bell & Pringle (1974), should be  $-2$ . Also, the subscript ‘1’ in  $R_1$  and  $M_1$

refers to the viscous time  $t_{\text{vis}} = 1$ , when the physical time  $t = 0$ .

## REFERENCES

- Alexander, D. R., & Ferguson, J. W. 1994, *ApJ*, 437, 879 [3](#)
- Angulo, C., Arnould, M., Rayet, M. et al. 1999, *Nucl. Phys. A*, 656, [3](#) [3](#)
- Baraffe, I., Chabrier, G., Allard, F., & Hauschildt, P. 2002, *A&A*, 382, 563 [1](#)
- Baraffe, I., Chabrier, G., & Barman, T. 2008, *A&A*, 482, 315 [2](#)
- Baraffe, I., Chabrier, G., Barman, T., Allard, F., & Hauschildt, P. 2003, *A&A*, 402, 701 [2](#), [6](#), [7](#), [10](#), [11](#)
- Bodenheimer, P., Hubickyj, O., & Lissauer, J. J. 2000, *Icarus*, 143, [2](#) [2](#), [3](#)
- Bonnefoy, M., Boccaletti, A., Lagrange, A.-M. et al. 2013, *A&A*, in press. arXiv:1302.1160 [10](#), [11](#)
- Bonnefoy, M., Lagrange, A.-M., Boccaletti, A. et al. 2011, *A&A*, 528, 15 [11](#)
- Burrows, A., Marley, M., Hubbard, W. B. et al. 1997, *ApJ*, 491, 856 [1](#), [2](#)
- D'Angelo, G., Durisen, R. H., & Lissauer, J. J. 2011, in *Exoplanets*, ed. S. Seager (Tucson, AZ: Univ. Arizona Press), 319 [4](#)
- D'Angelo, G., Henning, T., & Kley, W. 2002, *A&A*, 385, 647 [5](#)
- D'Angelo, G., Kley, W., & Henning, T. 2003, *ApJ*, 586, 540 [4](#), [5](#)
- D'Angelo, G., & Lubow, S. H. 2008, *ApJ*, 685, 560 [4](#), [5](#)
- D'Angelo, G., & Marzari, F. 2012, *ApJ*, 757, 50 [4](#), [13](#)
- Freedman, R. S., Marley, M., & Lodders, K. 2008, *ApJS*, 174, 504 [3](#), [6](#)
- Galvagni, M., Hayfield, T., Boley, A. et al. 2012, *MNRAS*, 427, 1725 [2](#)
- Greenzweig, Y., & Lissauer, J. J. 1992, *Icarus*, 100, 440 [2](#)
- Heney, L., Forbes, J., & Gould, N. 1964, *ApJ*, 139, 306 [2](#)
- Hubickyj, O., Bodenheimer, P., & Lissauer, J. J. 2005, *Icarus*, 179, 415 [2](#)
- Iaroslavtitz, E., & Podolak, M. 2007, *Icarus*, 187, 600 [2](#)
- Kippenhahn, R., & Weigert, A. 1990, *Stellar Structure and Evolution* (Berlin: Springer-Verlag) [2](#)
- Lagrange, A.-M., Bonnefoy, M., Chauvin, G. et al. 2010, *Science*, 329, 57 [11](#)
- Lagrange, A.-M., De Bondt, K., Meunier, N. et al. 2012, *A&A*, 542, A18 [11](#)
- Lagrange, A.-M., Gratadour, D., Chauvin, G. et al. 2009, *A&A*, 493, L21 [11](#)
- Lissauer, J. J., Hubickyj, O., D'Angelo, G., & Bodenheimer, P. 2009, *Icarus*, 199, 338 [2](#), [3](#), [5](#), [7](#), [12](#)
- Lissauer, J. J., & Stevenson, D. J. 2007, in *Protostars and Planets V*, ed. B. Reipurth, D. Jewitt, & K. Keil (Tucson: Univ. of Arizona Press), p. 591 [2](#)
- Lovis, C., Mayor, M., & Udry, S. 2006, in *Planet Formation*, ed. H. Klahr & W. Brandner (Cambridge UK: Cambridge Univ. Press), p. 203 [1](#)
- Lubow, S. H., & D'Angelo, G. 2006, *ApJ*, 641, 526 [5](#), [15](#)
- Lynden-Bell, D., & Pringle, J. E. 1974, *MNRAS*, 168, 603 [14](#), [15](#)
- Marleau, G.-D., & Cumming, A. 2013, arXiv:1302.1517 [11](#)
- Marley, M. S., Fortney, J. J., Hubickyj, O. et al. 2007, *ApJ*, 655, 541 [1](#), [2](#), [12](#)
- Marley, M. S., Saumon, D., Cushing, M. et al. 2012, *ApJ*, 754, 135 [11](#)
- Marois, C., Zuckerman, B., Konopacky, Q., Macintosh, B., & Barman, T. 2010, *Nature*, 468, 1080 [11](#)
- Mollière, P., & Mordasini, C. 2012, *A&A*, 547, A105 [2](#), [5](#), [6](#), [7](#), [8](#), [10](#)
- Mordasini, C. 2013, *A&A*, submitted [12](#)
- Mordasini, C., Alibert, Y., Klahr, H., & Henning, T. 2012, *A&A*, 547, A111 [2](#)
- Movshovitz, N., Bodenheimer, P., Podolak, M., & Lissauer, J. J. 2010, *Icarus*, 209, 616 [2](#), [3](#), [6](#), [7](#)
- Movshovitz, N., & Podolak, M. 2008, *Icarus*, 194, 368 [3](#)
- Peña Ramírez, K., Béjar, V. J. S., Zapatero Osorio, M. R. et al. 2012, *ApJ*, 754, 30 [1](#)
- Podolak, M. 2003, *Icarus*, 165, 428 [3](#)
- Podolak, M., Pollack, J. B., & Reynolds, R. T. 1988, *Icarus*, 73, 163 [2](#)
- Pollack, J. B., Hubickyj, O., Bodenheimer, P. et al. 1996, *Icarus*, 124, 62 [2](#), [4](#), [7](#)
- Pollack, J. B., McKay, C. P., & Christofferson, B. 1985, *Icarus*, 64, 471 [3](#)
- Potekhin, A. Y., & Chabrier, G. 2012, *A&A*, 538, A115 [3](#)
- Prodanović, T., Steigman, G., & Fields, B. D. 2010, *MNRAS*, 406, 1108 [3](#)
- Quanz, S. P., Meyer, M. R., Kenworthy, M. et al. 2010, *ApJ*, 722, L49 [11](#)
- Sahlmann, J., Segransan, D., Queloz, D. et al. 2011, *A&A*, 525, A95 [1](#)
- Salpeter, E. E. 1992, *ApJ*, 393, 258 [6](#)
- Saumon, D., Chabrier, G., & van Horn, H. M. 1995, *ApJS*, 99, 713 [3](#)
- Schneider, J., Dedieu, C., Le Sidaner, P. et al. 2011, *A&A*, 532, A79 [1](#)
- Spiegel, D. S., & Burrows, A. 2012, *ApJ*, 745, 174 [2](#)
- Spiegel, D. S., Burrows, A., & Milsom, J. A. 2011, *ApJ*, 727, 57 [1](#)
- Thompson, S. L. 1990, ANEOS—Analytic equations of state for shock physics codes (Sandia Natl. Lab. Doc. SAND89-2951) [2](#)
- Weidenschilling, S. J. 1977, *Astrophys. Sp. Sci.*, 51, 153 [7](#)